



Impact of a coupled ocean wave–tide–circulation system on coastal modeling

Il-Ju Moon *

Graduate School of Oceanography, University of Rhode Island, South Ferry Road, Narragansett, RI 02882, USA

Received 1 September 2003; received in revised form 26 January 2004; accepted 2 February 2004

Available online 20 February 2004

Abstract

The impact of a coupled ocean wave–tide–circulation system on coastal modeling for wind waves, oceanic circulation, and water-mass simulation is investigated by coupling of two well-tested models: the third-generation wave model (WAVEWATCH-II) and the Princeton ocean model (POM). In this study, several numerical experiments in the Yellow and East China Sea (YECS) are performed for the ideal winter case and the typhoon Winnie case. In the coupled system, wind waves are influenced by both currents and sea level elevation induced by tides, storm surges, and oceanic circulation. Tides were the most influential factor in modulating mean wave characteristics in the YECS. The magnitude of the modulation of mean wave parameters at neap tides is found to be half that at spring tides. In the YECS the tides affect not only wind waves, but also seasonal circulation and water-mass distributions. Tides increase the bottom friction of the YECS significantly and this contributes to a change of winter current direction up to 60 °C in the YECS and a decrease of surface temperatures along the trough of the Yellow Sea up to 4 °C in winter. Tides in summer produce the strong vertical mixing in shallow regions. This leads to the formation of tidal fronts in a boundary between well-mixed and stratified regions and causes sea surface temperatures (SST) along the west coast of Korea decrease as much as 3 °C. Effects of ocean waves on coastal circulation and SST simulations are investigated considering wave-dependent stress, wave breaking parameterization, and Langmuir circulation under typhoon Winnie conditions. The results show that the wave-dependent stress, which is strongly dependent on wave age and relative position from storm center, as well as the wave breaking have the most significant impact on the SST distribution.

© 2004 Elsevier Ltd. All rights reserved.

Keywords: Wave model; Oceanic model; Circulation; Tides; Waves; Coupling; Interaction; Stress

* Tel.: +1-401-874-6508; fax: +1-401-874-6728.

E-mail address: mij@gso.uri.edu (I.-J. Moon).

1. Introduction

In coastal and shelf regions, tides, storm surges, wind waves and oceanic circulation are the main processes that determine the physical environment of the region and are major components of marine forecasts. It has been known that these processes coexist in many cases and their interactions are very important for individual dynamic processes (Longuet-Higgins and Stewart, 1960; Prandle and Wolf, 1978; Janssen, 1992; Bao et al., 2000; Welsh et al., 2000). Although there have been a number of studies on the individual processes for the last decades, how these processes influence one another is still an important issue in coastal modeling.

It is believed that wind waves have a significant influence on sea surface stress (or roughness) that generates currents in storm surge and coastal circulation modeling (Smith et al., 1992; Janssen, 1992; Mastenbroek et al., 1993). From measurements in the North Sea, Smith et al. (1992) found that the sea surface roughness decreases as wave age increases. Janssen (1989, 1991, 1992) pointed out that wave-induced stress in young wind seas might be a substantial amount of the total stress in the surface layer, resulting in a considerable enhancement of the drag of airflow. Based on the theory of Janssen (1991), a number of storm surge models have considered the effect of ocean waves on storm surge predictions (Mastenbroek et al., 1993; Zhang and Li, 1996, 1997; Moon et al., 2003b).

An important role of surface waves is to act as a significant barrier to the exchange of heat and gases between ocean and atmosphere. The momentum enters the surface wave fields first and is transmitted to the surface current field mainly by wave breaking. The wave breaking enhances turbulent kinetic energy that is responsible for mixing the momentum down through the water column (Drennan et al., 1992). Therefore, wave breaking has a considerable effect on the near-surface distributions of oceanic mixed layer (OML) properties, such as velocity, temperature, and salinity, affecting ocean circulation modeling (Craig and Banner, 1994; Kantha and Clayson, 2004; Mellor and Blumberg, 2004).

Surface waves are also responsible for producing Langmuir circulations, which are formed due to the interaction of the wind-driven surface shear with the Stokes drift of the surface waves (Craik and Leibovich, 1976). It has been known that the Langmuir circulations play a role in mixing in the upper ocean and vertical transfer of momentum, and are able to rapidly destroy the surface thermal stratification in shallow diurnal mixed layer (Weller and Price, 1988; Kantha and Clayson, 2004). Thus, Langmuir circulations are undoubtedly important to the oceanic mixed layer modeling in ocean circulation.

Ocean circulations including storm surges, tides, and oceanic currents, on the other hand, have a significant effect on a wave field if the effects of their currents and elevations are big enough. Tolman (1991) described the effect of tides and storm surges on wind waves for three North Sea storms cases and showed that tides and storm surges should be considered as unsteady mediums for wind wave propagation if wave–current interactions are assessed. Holthuijsen and Tolman (1991) and Komen et al. (1994) indicated that oceanic currents such as the Gulf Stream, the Kuroshio, and the Agulhas current, also influence wave fields of the regions.

In coastal areas with strong tides, tides are an important factor affecting storm surges and ocean circulations. Tang et al. (1996) demonstrated that a nonlinear interaction between the storm surge and the tides affects strongly the prediction of coastal sea levels and is predominantly caused by the quadratic bottom friction. Lee (1999) emphasized the importance of M_2 tide in the

circulation of the East China Sea. Simmons et al. (2004) suggested that the incorporation of tidal mixing parameterization into the ocean general circulation leads to improving the representation of the ocean mixing processes. Schiller (2004) pointed out that tidal currents play an essential role in transport and mixing processes in the Indonesian Seas.

Because of the importance of such environmental interactions, accurate coastal modeling strongly needs the dynamically coupled system of two or more processes. Recently, several coupling experiments in coastal areas have been studied (Tolman, 1991; Mastenbroek et al., 1993; Davies and Lawrence, 1995; Zhang and Li, 1996; Xie et al., 2001, 2003; Choi et al., 2003). Their main interests were interactions between the storm surges (or tides; or wind-driven currents) and wind waves using a coupled storm surge and wave model. Mastenbroek et al. (1993) and Zhang and Li (1996) investigated wave effect in aspects of storm surge modeling; Tolman (1991) described the effects of tides and storm surges on wave modeling; Davies and Lawrence (1995) and Xie et al. (2001, 2003) investigated the effects of wave–current interaction on wind-driven currents. However, these were not fully coupled coastal modeling studies because their ocean circulation models produce only wind-driven (or tide-driven) circulation, not considering variations of water temperature and salinity as well as volume transport and river input. In some cases, the coupling was only one-way.

Water temperature, especially sea surface temperature (SST), is an important factor to be considered in coastal coupling studies because it is very sensitive to the dynamic response of air–sea interaction and consequently affects both the atmospheric and oceanic systems. Impact of SST on hurricane intensity forecasts is a good example that emphasizes its importance in the air–sea interaction. Bender and Ginis (2000) show that a decrease of SST due to entrainment of the cooler waters from the thermocline in the mixed layer under hurricane wind forcing produces a significant change of storm intensity. SST changes are strongly dependent on the surface momentum flux and an upward enthalpy flux across the interface in the upper ocean, which are determined either by changes in the atmospheric forcing and changes in the ocean circulation. Therefore, SST can have large variability on a wide range of temporal spatial scales resulting from changes in tides, ocean waves, and storm surges.

A fully coupled system of atmospheric model, wind-wave model, and ocean circulation model is the ultimate goal in environmental modeling research and operational forecasting. Bao et al. (2000) studied air–sea interactions with such a system for the first time. They successfully introduced the roles of ocean mixing, sea spray and sea-surface waves on air–sea interaction under high wind conditions with the coupled atmosphere–wave–ocean modeling system, although they left further studies on two-way coupling system between an ocean circulation model and a wind-wave model, which is not included yet in their model. Indeed, the coupling of ocean circulation and wind-wave model is involved with very important dynamics at the ocean surface and bottom boundaries, such as, air–sea momentum flux modifications (induced by waves and sea spray), wave–current interactions, and upper ocean (or bottom) mixing processes (induced by tides, storm surges, Stokes drift, Langmuir circulations, and breaking waves). While these processes were well studied for the last decades, there are still many uncertainties in estimating the effects quantitatively, which have resulted in making a full coupling of ocean circulation and wind-wave model difficult.

In the present study, we developed a coupled ocean wave–tide–circulation system, which takes into account major physical features of coastal seas (such as realistic tides, wind waves, storm

surges, oceanic currents, surface heat flux and fresh water input) and major coupling processes (such as wave-induced surface momentum exchanges, wave–current interactions, tide-induced mixing processes, Langmuir circulations, and mixing processes by breaking waves). This study does not aim to investigate all mechanisms involving the coupling of ocean circulation and wind-wave models, or to include them in the coupled model. It focuses on investigating interactions among major physical processes in coastal regions with well-established coupling mechanisms and how the interactions affect the realistic coastal simulation. The first part of this paper examines wind waves interacting with tides, storm surges, and oceanic circulations. The impact of these interactions on the coupled system is investigated through a series of numerical experiments in the Yellow and East China Sea (YECS). In the second part, the effect of tides and wind waves on the circulation and water-mass distributions of the YECS is evaluated within the coupled system.

The models used in the coupled system and their coupling processes are described in Section 2. Detailed descriptions of model areas, experimental designs, and data sets for numerical experiments are given in Section 3. Effects of the coupled system on wind waves and coastal circulation simulations are investigated in Sections 4 and 5. Summary and conclusion are given in the last section.

2. Coupled ocean wave–tide–circulation system

2.1. Model descriptions

The coupled ocean wave–tide–circulation system used in this study is based on the synchronous coupling of two well-tested models: a third-generation wave model (WAVEWATCH-II) and a Princeton ocean model (POM). WAVEWATCH-II (WW) was developed at the NASA Goddard Space Flight Center in the spirit of the WAM (WAMDI group, 1988), but is designed with more general governing transport equations allowing incorporation of unsteady and inhomogeneous currents on ocean waves, which permit full coupling with ocean models. Updated versions of the WW have been used for research and operational applications worldwide (Tolman, 2002; Moon et al., 2003a). WW has the characteristics of a third-generation approach to wave growth and decay, explicitly accounting for wind input, wave–wave interaction and dissipation due to whitecapping and wave–bottom interaction. The source terms of WW use the wind input expressed by Cavaleri and Rizzoli (1981) and Janssen (1991), the nonlinear wind–wave interaction of Hasselmann and Hasselmann (1985), the dissipation by Janssen (1991), and the bottom friction based on the JONSWAP parameterization as in most WAM models (Hasselmann et al., 1973). A detailed description of the model was given by Tolman (1989, 1991) and Moon (2000).

The present version of WW has a regularly spaced longitude–latitude grid of $1/6^\circ$ -by- $1/6^\circ$ resolution, extending from 22°N to 42°N and from 117°E to 132°E . The model-resolving minimum water depth is 2 m and the time step is 1800 s. The wave spectrum is discretized using 24 directions ($\Delta\theta = 15^\circ$) and 26 frequencies extending from 0.041 to 0.453 Hz with a logarithmic increment $f_{n+1} = 1.1f_n$, where f_n is the n th frequency. The bathymetry of the model domain is shown in Fig. 1. The model provides the point outputs for directional wave spectra and the gridded outputs for mean wave parameters such as significant wave heights, $H_s (= 4\sqrt{E})$, mean

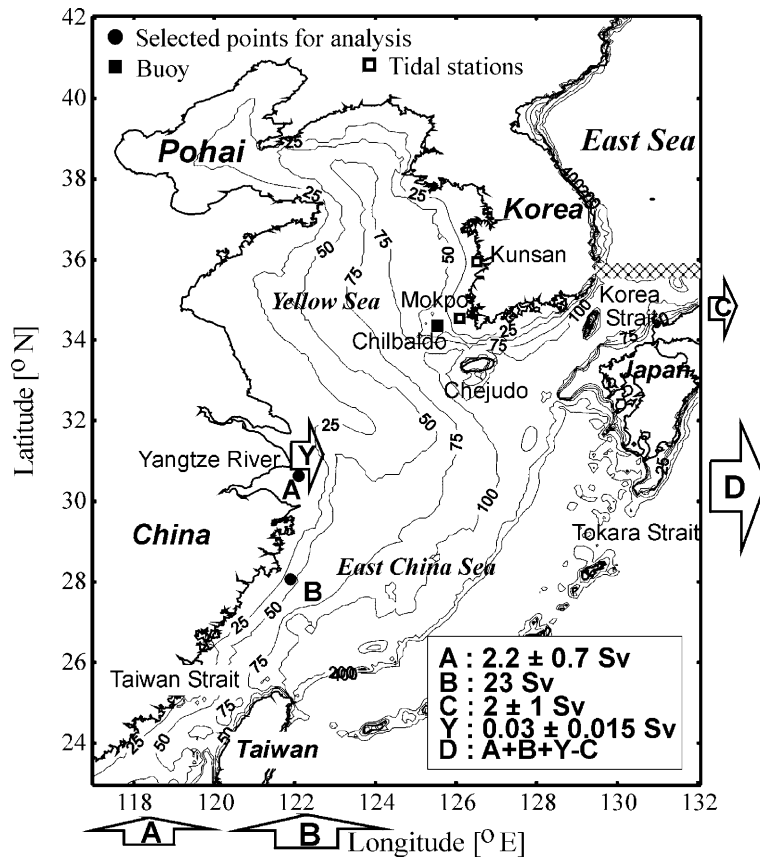


Fig. 1. Bathymetry of the Yellow and East China Seas and the volume transport at the open boundaries and Yangtze River mouth. The unit for volume transport is Sv ($= 10^6$ m³/s) and isobaths are in meters. Station 'A' is a point where tides are strong. Station 'B' is a point, in which both of tides and typhoon influence. Kunsan and Mokpo are tidal stations and Chilbaldo is a buoy station.

wavelengths, L ($= 2\pi\overline{k^{-1}}$), mean absolute wave periods, T_a ($= 2\pi\overline{\omega^{-1}}$), and mean relative wave periods, T_r ($= 2\pi\overline{\sigma^{-1}}$). Here, E is the spectrum energy, σ is the relative frequency (as observed in a frame or reference moving with the mean current U), ω is the absolute frequency (as observed in the fixed frame), and k is the wavenumber (which is related to the frequencies σ and ω in the dispersion relation, $\sigma = \omega - k \cdot U$).

POM (Blumberg and Mellor, 1987) is a free-surface, sigma-coordinate, and primitive equation model including a Mellor and Yamada (1982) (henceforth, M–Y) turbulent closure submodel to provide vertical mixing coefficients. In this study, POM employs an additional turbulent closure submodel that is a modified version of M–Y model (Craig and Banner, 1994; Mellor and Blumberg, 2004) to investigate the wave breaking effect on the upper ocean mixing (see Section 2.4). POM has the same grid and resolution as the wave model, but has three inflows at open boundaries; the shelf break east of Taiwan, the Taiwan Strait and the Yangtze River with volume transports of 23, 2.2 ± 0.7 , and 0.030 ± 0.015 Sv, respectively (Fig. 1). Along the boundaries, tidal

and atmospheric pressure-gradient forcings are also specified according to a radiation condition originally due to Flather (1976). Tides are expressed by using eight tidal constituents (M_2 , S_2 , K_1 , O_1 , K_2 , N_2 , P_1 , and Q_1). The heat exchange across the sea surface between the ocean and atmosphere is expressed by an empirical formula of Edinger et al. (1974) using the heat exchange coefficient and the equilibrium temperature. Full details of the input data for winds and heat fluxes are given in Moon (2000).

2.2. Wave–current coupling in wave model

WW uses the action density spectrum, which is directly related to the energy spectrum or variance density spectrum and conserved during propagation (Whitham, 1965; Bretherton and Garrett, 1968). This leads to the corresponding basic balance equation for the action spectrum (A) considering wave–current interaction (WAMDI group, 1988; Tolman, 1991):

$$\frac{\partial A}{\partial t} + \overbrace{\nabla_x \cdot [(\dot{c}_g + \vec{U})A]}^a + \overbrace{\frac{\partial}{\partial \omega} [\dot{c}_\omega A]}^b + \overbrace{\frac{\partial}{\partial \theta} [\dot{c}_\theta A]}^c = \frac{S}{\sigma}, \quad (1)$$

$$\dot{c}_g = \frac{\sigma}{k} \left[\frac{1}{2} + \frac{kd}{\sinh 2kd} \right], \quad (2)$$

$$\dot{c}_\omega = \frac{\partial \sigma}{\partial d} \frac{\partial d}{\partial t} + \vec{k} \cdot \frac{\partial \vec{U}}{\partial t}, \quad (3)$$

$$\dot{c}_\theta = -\frac{1}{k} \left[\frac{\partial \sigma}{\partial d} \frac{\partial d}{\partial m} + \vec{k} \cdot \frac{\partial \vec{U}}{\partial m} \right], \quad (4)$$

where S is the net source term for wave variance, U is the mean current velocity, d is the water depth (sum of mean water depth, H , and sea level elevation, η), σ is the relative frequency, θ is the direction normal to the wave crests, c_g is the velocity of wave energy propagation, c_ω and c_θ are the propagation velocities in the corresponding spaces, and m is a coordinate perpendicular to θ . In the coupled system, WW uses new information on surface currents (U) and water elevations (η) fed back from POM. In (1), U and η are used to calculate the straining effect of the wave field due to spatial variation of $c_g + U$ (a on LHS), the change of absolute frequency due to the unsteadiness of depth and current (b on LHS), and the change of wave direction due to the depth- and current-induced refraction (c on LHS).

2.3. Coupling through wave-dependent surface stress

POM uses the surface stress calculated from WW to consider the effect of surface waves on the wind stress. Following Janssen (1991), the total surface stress (τ) is expressed by the sum of the wave-induced stress (τ_w) and the turbulent stress (τ_t). τ_t is parameterized with a mixing-length hypothesis and τ_w is given by

$$\tau_w = \rho_w \int_0^\infty \int_0^{2\pi} \sigma S_{\text{in}}(f_r, \theta) df d\theta. \quad (5)$$

Here, S_{in} is the input source term of WW (Janssen, 1991), f_r is $\sigma/2\pi$, and ρ_w is water density. The corresponding wind profile is given by

$$U(z) = \frac{u_*}{\kappa} \ln \left(\frac{z + z_e - z_0}{z_e} \right), \quad (6)$$

where u_* is the air side friction velocity, z_0 is the roughness length in the absence of waves, and z_e is the effective roughness. z_e and z_0 are given by

$$z_e = \frac{z_0}{\sqrt{1 - \tau_w/\tau}}, \quad (7)$$

$$z_0 = 0.01 \frac{u_*}{g}. \quad (8)$$

Here, (8) is a Charnock type relation, tuned to give correct stresses for old wind waves. These equations, (5)–(8), can be solved iteratively if the wind speed at $z = 10$ m is given.

The momentum transfer from atmosphere to ocean consists of two components due to the presence of waves: momentum transferred directly into the ocean current and momentum transferred to the waves. The momentum to the waves then is partly dissipated in the surface ocean current. In this study, it is assumed that the dissipated wave momentum and the part of the total stress left by subtracting wave-induced stress (i.e., turbulent stress) is transferred to the ocean current. The dissipated wave momentum is evaluated by integrating the product of the wave momentum dissipation rate (related to the wave dissipation rate that is internally parameterized in WW) and the spectrum of the surface wave field.

2.4. Wave-breaking parameterization

In the past, it was believed that the law of the wall, in which the velocity profile is logarithmic and energy dissipation decays inversely with depth, prevails near the interface. Recent measurements, however, demonstrated the existence of a sublayer with very high dissipation rate within meters of the surface, in which turbulence is enhanced by the action of surface wave breaking (Terray et al., 1996; Drennan et al., 1996). In this layer, the dissipation appears to decay inversely with depth raised to a power estimated between 2 and 4.6 (Gargett, 1989; Craig and Banner, 1994; Terray et al., 1996; Drennan et al., 1996).

The well-known M–Y turbulence closure model has ignored that these breaking waves create additional turbulence and mixing. Effect of wave breaking on mixing in the oceanic mixed layer may play a significant role in the present coupled model. In this study, we employed an additional turbulence closure model to test the wave breaking effect, using the level $2^{1/2}$ turbulence closure scheme of M–Y modified by Craig and Banner (1994) (henceforth, C–B).

Following C–B and Mellor and Blumberg (2004) (henceforth, M–B), a new boundary condition for the turbulent kinetic energy equation is suggested by

$$q^2 = (15.8\alpha_{CB})^{2/3} u_\tau^2 \quad \text{at } z = 0, \quad (9)$$

$$l = \max(\kappa z_w, l_z) \quad \text{at } z = 0, \quad (10)$$

$$z_w = 0.85H_s, \quad (11)$$

where $q^2/2$ is the turbulent kinetic energy, z is vertical coordinate, u_τ is the water side friction velocity, α_{CB} is a constant, g is the gravity acceleration, l is the so-called master length scale, l_z is the ‘conventional’ empirical length scale associated with M–Y model (M–Y, 1982; M–B, 2004), κ is von Karman’s constant, and H_s is the significant wave height.

M–B used the constant α_{CB} and z_w for sensitivity tests of M–Y model. These parameters, however, can be estimated from the wave model more precisely, since α_{CB} and z_w requires knowledge of the wave spectrum and H_s , respectively. Following Terray et al. (1996) and M–B (2004), α_{CB} is determined by

$$\alpha_{CB} = \frac{F}{u_\tau^3}, \quad (12)$$

where F is the rate of energy input to the waves from the wind, which is defined as the integral of the growth rate, β , over the wave spectrum. In WW, F is parameterized, based on the expression of Janssen (1991), as

$$F = \int \int \beta \frac{\rho_a}{\rho_w} \left(\frac{u_*}{c} \right)^2 \max[0, \cos(\theta - \theta_w)]^2 \sigma \psi(f_r, \theta) df_r d\theta, \quad (13)$$

where $\psi(f_r, \theta)$ is the frequency–direction spectrum of the waves, ρ_a is air density. θ_w is the mean wind direction, c is the phase velocity, and β is the Miles constant, which is estimated from the non-dimensional critical height λ using z_c in Eq. (7).

2.5. Inclusion of Langmuir circulations

Langmuir circulations are formed due to the interaction of the wind-driven surface shear with the Stokes drift of the surface waves. In order to include the effect of Langmuir circulations on ocean circulation model, the governing momentum equations are modified by the appearance of a vortex force term as well as inclusion of Stokes drift in Coliolis term (McWilliam et al., 1997; Kantha and Clayson, 2004). In Eqs. (3) and (4) of Mellor (2003b), the Coliolis terms are modified as

$$-fV = -f(V + v_s), \quad +fU = +f(U + u_s), \quad (14)$$

and the vortex force term, $\vec{u}_s \times (\nabla \times \vec{u})$, is added on RHS of the equations as

$$v_s \left(\frac{\partial v}{\partial x} - \frac{\partial u}{\partial y} \right), \quad u_s \left(\frac{\partial v}{\partial x} - \frac{\partial u}{\partial y} \right). \quad (15)$$

The quantities, u_s and v_s are components of the Stokes drift velocity, \vec{u}_s , whose magnitude is given by

$$|\vec{u}_s| = (u_s^2 + v_s^2)^{1/2} = c(ka)^2 \exp(2kz), \quad (16)$$

where c is the wave phase speed, k is the wave number, z is the depth, and a is the amplitude. In real ocean wave fields the Stokes drift velocity can be calculated from the integral of the Stokes drift components over all directions and frequencies as

$$u_S(z) = \int_0^{2\pi} \int_0^\infty ck^2 \psi(f_r, \theta) \exp(2kz) \cos \theta df_r d\theta, \quad (17)$$

$$v_S(z) = \int_0^{2\pi} \int_0^\infty ck^2 \psi(f_r, \theta) \exp(2kz) \sin \theta df_r d\theta. \quad (18)$$

2.6. Coupling procedure

Using the above coupling parameterizations for wave–current interactions, surface stress, wave breaking, and Langmuir circulations, the coupling of WW and POM takes place in the following sequence. During the first time step, WW calculates the directional wave spectrum and significant wave height with wind inputs (but, without consideration of current and elevations). The outputs are then used to estimate the sea surface stress (by Eqs. (5)–(8)), wave breaking parameterization (by Eqs. (9)–(13)), and the Stokes drift (by Eqs. (14)–(18)). These coupling values are then entered into POM to obtain currents and elevations. In the next time step, the currents and elevations are passed to WW to compute new wave fields. This process is repeated. Here, the two-way coupling takes place every 1800 s. In the calculation of surface stresses, the present approach allows only for a stability-independent estimate, since it excludes the coupling with the atmospheric model (Bao et al., 2000).

3. Numerical experiments

3.1. Experimental design

The effect of the coupled ocean wave–tide–circulation system on coastal modeling for wind waves, oceanic circulation, and water-mass simulation is investigated through a series of numerical experiments (Table 1). In wave modeling experiments (A_T , A_S , A_K , and A_A), modulations of mean wave parameters induced by tides (T), storm surges (S), ocean circulation (K), or all of these processes (A) are examined. For each process, the effect of currents and elevations on the mean wave parameters is examined ($A1$, $A2$, $A3$, and $A4$). In coastal circulation and water-mass modeling, the effect of tides is investigated focusing on seasonal variations by two experiments (B1, B2) with and without tidal effect. The effect of wind waves is examined over a typhoon event by four experiments (C1–C4) with two different types of wind stress formulas and inclusion of wave breaking and Langmuir circulation.

Analysis of experimental results for wind waves mostly consists of two parts: (i) the spatial distribution of the modulations induced by interactions among the processes and (ii) the time series of modulated parameters at selected locations where strong mutual interactions of two or more processes exist. This paper does not cover to examine the effect of tides and wind waves on storm surge modeling. This is given in Moon and Oh (2003).

The Yellow and East China Sea (YECS) are characterized by extreme and various physical phenomena, such as strong tidal currents, frequent storm surges, high wind waves, and strong oceanic currents. For this reason they are selected for the present numerical experiments. Two cases representing the synoptic characteristics of summer and winter in these areas are applied to

Table 1
Summary of numerical experiments

Simulation	Experimental name	Experimental descriptions
Wind waves	A1 _{T,S,K,A}	Coupled simulation, which considers both currents and elevations induced by one of the following, tides (T), storm surges (S), ocean circulation (K), or all of processes ($A = T+S+K$)
	A2 _{T,S,K,A}	The same as A1, but without considering currents, i.e. elevations are only considered here
	A3 _{T,S,K,A}	The same as A1, but without considering elevations, i.e. currents are only considered here
	A4 _{T,S,K,A}	Uncoupled simulation without considering both of currents and elevations
Coastal circulation and water-mass	B1	Monthly mean simulation, which considers wind, heat flux, river input and tides
	B2	The same as B1, but without considering tides
	C1	Simulation for typhoon Winnie, which considers wind, heat flux, river input, tides as well as a coupling through wave-dependent surface stress. Janssen's (1991) approach is used to calculate the surface wind stress
	C2	The same as C1, but without a coupling through wave-dependent surface stress. Wu's (1982) drag relationship, $C_d = (0.8 + 0.065W) \times 10^{-3}$, is used to calculate the surface wind stress
	C3	The same as C1, but with Langmuir terms in momentum equations
	C4	The same as C1, but with both wave breaking effects in TKE equations and Langmuir terms in momentum equations. This is a fully coupled simulation

the experiments for wind waves and coastal circulation modeling: Case I, an ideal winter condition with a constant 14 m/s northwesterly winds and Case II, situation during the typhoon Winnie, which struck the eastern coast of China during 16–23 August 1997. The tidal effect on circulation in the YECS focuses on the seasonal variation.

3.2. Data

Seasonal circulation of the YECS is simulated using 18-year-monthly-mean winds (Na and Seo, 1998), Levitus (1982) data, and the Comprehensive Ocean–Atmosphere Data Set (COADS). Levitus (1982) data are used for temperature and salinity profiles at inflow boundaries of the Taiwan Strait and the east strait of Taiwan. Heat exchange quantity across the air–sea interface is calculated using the COADS. Simulation of circulation and water-mass during the passage of typhoon Winnie uses the model outputs of atmospheric variables (6-h interval), which are calculated routinely from the Regional Data Assimilation and Prediction System (RDAPS) at the

Korean Meteorological Administration (KMA). Measured mean wave parameters (3-h interval) were obtained from a buoy located at Chilbaldo (Fig. 1).

4. Impact of the coupled system on wind waves modeling

4.1. Effect of tides

The effect of tides on wind waves are examined by four numerical experiments, A1_T, A2_T, A3_T, and A4_T (Table 1) for Case I. In these experiments, typical spring tides of the YECS are applied using eight tidal components. Fig. 2a and b show the ellipse and the coamplitude–cophase lines for a predominant tidal constituent in this area (M₂ tide). Maximum velocities and amplitudes of the tide are found on the west coasts of Korea, near the Yangtze River mouth of China, and at the Taiwan Strait. Tidal ellipses and coamplitude lines of other tidal components simulated from the present model and comparisons with observations for each tidal component are given by Moon (2000) and Moon et al. (2000). Considering local effects of wave–current interactions such as local Doppler shift, current velocity in the mean propagation direction of the waves is a more interesting parameter than overall current velocity (V). The current velocity in the mean propagation direction of the waves (V_{pro}) is defined here as

$$V_{\text{pro}} = |V| \cos(\theta_w - \theta_c), \quad (19)$$

where θ_w is the mean propagation direction of the waves and θ_c is the current direction. Fig. 2c, which is the spatial distribution of maximum V_{pro} during a tidal cycle for Case I, shows that the largest following current speeds occur around the Yangtze River mouth and in the eastern Yellow Sea. They are also concentrated to a somewhat lesser extent along the northeastern part of the Pohai. Under the influence of both tidal current and elevation (A1_T), the simulated significant wave height (H_s) and mean wavelength (L) are shown in Fig. 3a, where maximums reach 4 m for H_s and 120 m for L .

In order to estimate the spatial distribution of tidal effect on mean wave parameters (H_s , T_a , and L) during a certain period, a normalized local root mean square (RMS) of difference between two experiments is obtained at every grid points. For example, the normalized local RMS difference (NRD) between A1_T and A4_T for H_s is defined as

$$\text{NRD}(H_s) = \frac{\sqrt{\frac{1}{N} \sum (H_s^{\text{A1T}} - H_s^{\text{A4T}})^2}}{\frac{1}{N} \sum H_s^{\text{A4T}}}, \quad (20)$$

where N is the number of data points. NRDs for the other wave parameters (T_a , T_r , and L) are determined in the same way.

The distributions of NRD between A1_T and A4_T, which imply the combined effect of tidal elevations and currents on mean wave parameters, are presented in Fig. 3b–d. Here, the NRDs have been determined for a tidal cycle. The figures show that the combined tidal effect reach up to 11% in both T_a and L (Fig. 3b and d) and up to 7% in H_s (Fig. 3c), and the areas where strong wave–tide interactions exist (shaded areas) correspond to those with large amplitude (>100 cm) in Fig. 2b and with strong V_{pro} in Fig. 2c.

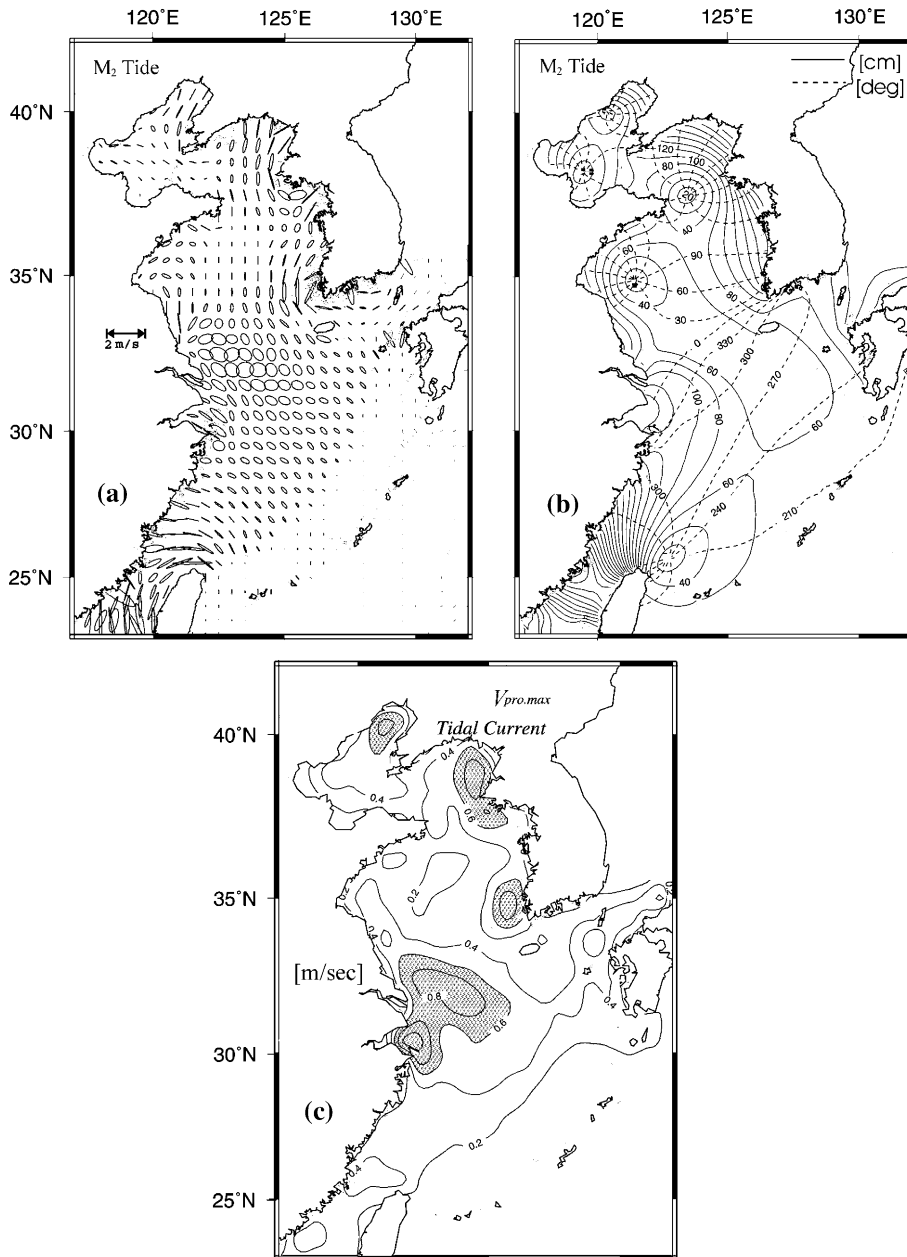


Fig. 2. (a) Tidal ellipses for M_2 tide. (b) Lines of coamplitude (solid lines) and cophase (dashed lines) for M_2 tide referred to 135°E. (c) Spatial distribution of maximum V_{pro} for a tidal cycle. Shaded areas are $V_{pro} > 0.6$ m/s.

Contribution of tidal current and elevation to wind waves can be estimated from a time series of mean wave parameters through four sensitivity experiments, A1_T, A2_T, A3_T, and A4_T. Fig. 4a–c shows the time series of the simulated H_s , T_a and L for the experiments at station ‘A’

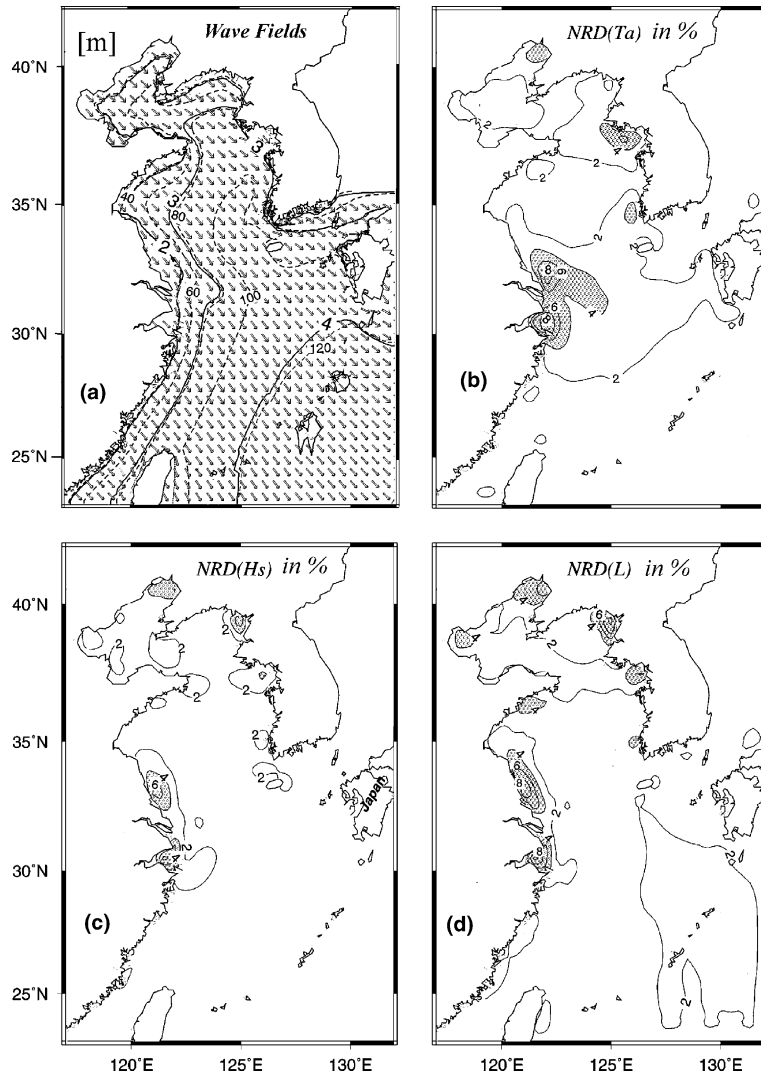


Fig. 3. (a) Simulated wave fields for Case I. Solid contours are significant wave heights, dashed contours are mean wavenumber, and arrows are mean wave directions. (b–d) Spatial NRD distributions between $A1_T$ and $A4_T$ for T_a , H_s , and L . Shaded areas are $\text{NRD} > 4\%$.

where the strongest wave–tide interaction exists (see Figs. 1 and 3b–d). The combined effect of tidal elevations and currents is assessed by comparing the solid ($A1_T$) and dashed ($A4_T$) lines. The effect is distinct in all mean wave parameters considered here and is dominated by both local currents and sea levels with a clear modulation of the tidal period. Eqs. (3) and (4) suggest that variations of depth (or elevation) and current in space result in changes of wave direction, whereas variations of those in time result in changes of absolute frequency. Increase in water depth reduces energy dissipation at the bottom boundary layer and produces larger and longer waves (Tolman, 1990). A current opposite the propagation direction of waves makes

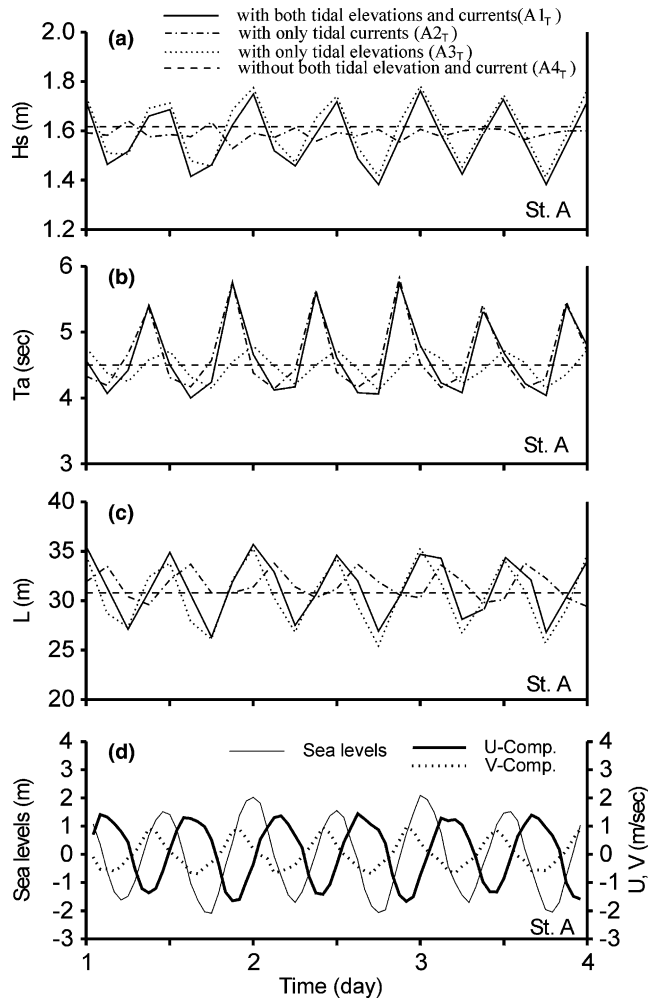


Fig. 4. (a–c) Time series of H_s , T_a , and L simulated from four experiments ($A1_T$, $A2_T$, $A3_T$, and $A4_T$) for Case I at station 'A'. (d) Variations of tidal levels and current components (U and V) during simulations.

wavelength shorter and wave height higher (Oh and Kim, 1992). These patterns correspond to those of Fig. 4. From a close of examination of these figures, it is also concluded that modulations of T_a are dominated mainly by local currents, whereas those of H_s and L are dominated by local depth.

Wave modulations induced by tides may depend on tidal strength and wind speeds. This is examined by additional experiments, which are the same as $A1_T$ and $A4_T$ except using different wind inputs (7 and 28 m/s) and tidal strength (neap tides). At station 'A' where strong wave–tide interaction exists, Table 2 shows that the tide-induced wave modulations for H_s decrease with increasing severity of wind condition, and that the difference of modulation between spring and neap tides is approximately 50%.

Table 2

Modulation of significant wave height depending on wind speed (7, 14, and 28 m/s) and strengths of tides (spring and neap tides) during a tidal cycle at station ‘A’

Wind speed (m/s)	Modulation [NRD, %]	
	Spring tides	Neap tides
7	5.4	2.8
14	4.2	2.1
28	3.5	1.6

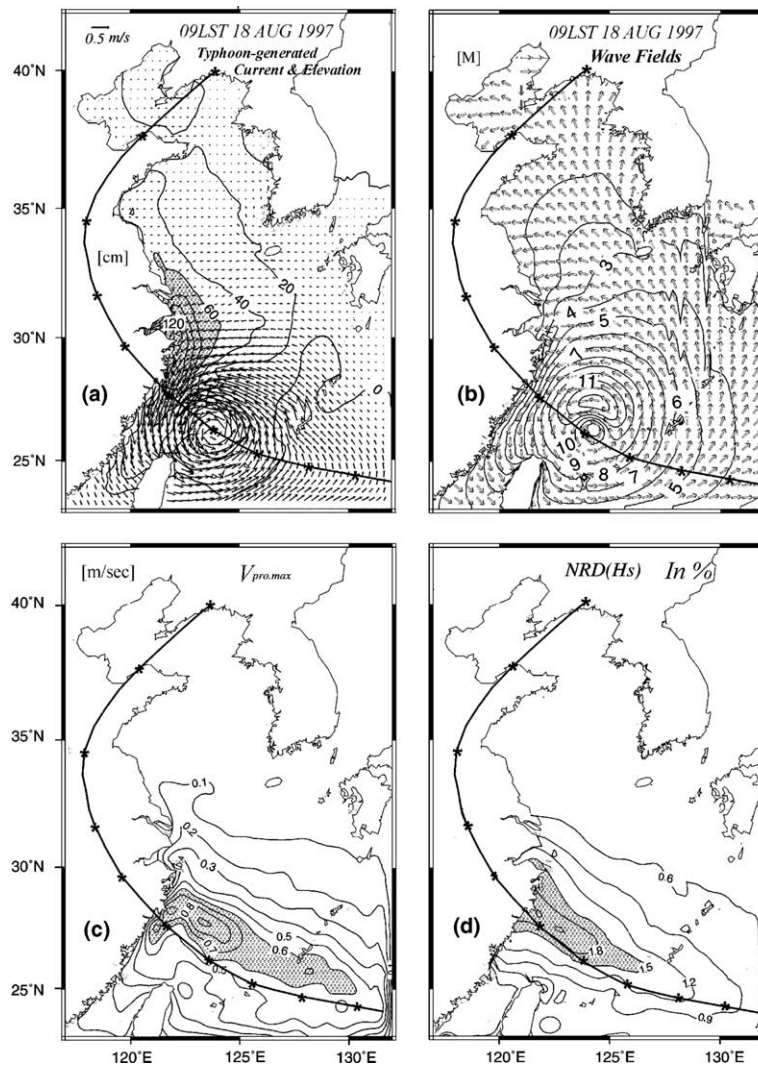


Fig. 5. (a–b) Spatial distributions of surface currents and waves driven by typhoon Winnie at 09h LST, 18 August 1997. Contours in (a) and (b) represent surge elevations and H_s , respectively; arrows in (a) and (b) represent current vectors and mean wave directions; a solid line with star mark is the storm track. (c,d) Distribution of maximum V_{pro} and NRD between $A1_s$ and $A4_s$ for H_s during Winnie event. Shaded areas are $V_{pro} > 0.6$ m/s and NRD > 1.5%, respectively.

4.2. Effect of storm surges

To investigate the effect of storm surges on wind waves, a typhoon Winnie event (Case II) is applied to four numerical experiments, A1_S, A2_S, A3_S, and A4_S (Table 1). In these experiments, the wind and pressure fields obtained from the RDAPS are only used as a surface forcing to generate currents. Fig. 5a shows the typhoon-generated surface current and elevation fields when Winnie approaches the East Coast of China. Here, the strongest currents appear to the right of the storm track and the highest surge is found in the southern part of the Yangtze River mouth. At this time, the simulated H_s reaches about 14 m (Fig. 5b). Fig. 5c, which is the spatial distributions of maximum V_{pro} for Case II, shows that the largest V_{pro} occurs along the storm track, especially to the right of the track. The NRD distribution of H_s for the combined effect of surge elevations and currents (i.e., A1_S versus A4_S) is presented in Fig. 5d. Here, the effect of wave–surge interaction on H_s is less manifest than that of tides. The maximum NRD is below 3%. The NRD distributions of T_a , T_r and L are similar to those of H_s (not presented here). The smaller contribution of storm surge to wave modulations than tides is because the influence of surge elevation is opposite to that of current, so they partially cancel out, reducing the intensity of surge–wave interaction (Tolman, 1990).

4.3. Effect of oceanic circulation

To estimate the effect of oceanic circulation on wind waves, four numerical experiments, A1_K, A2_K, A3_K, and A4_K, are performed under Case I conditions. Here, the oceanic circulation is generated from monthly-mean diagnostic simulation for February. The main circulation system in the YECS consists of the Kuroshio, the Taiwan current, and the Korean strait current. These currents all flow to the northeast (arrows, in Fig. 6a). If typical wind fields of winter in the

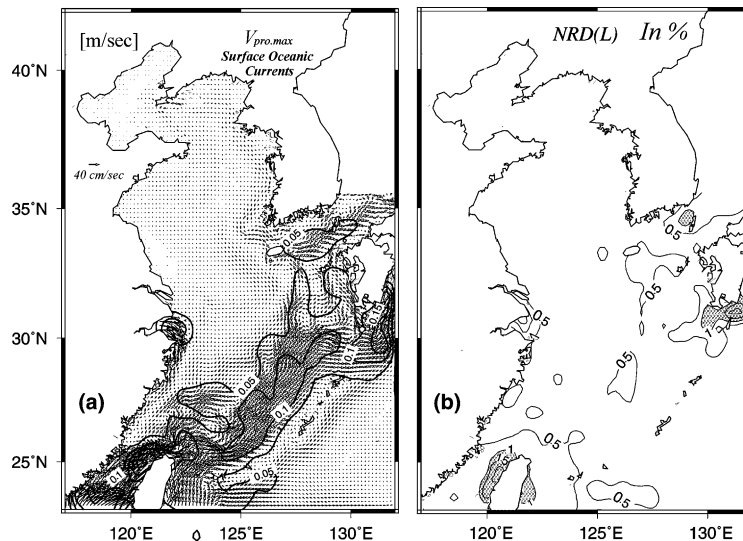


Fig. 6. (a) Spatial distributions of surface oceanic currents (arrows) on February in the YECS and their maximum V_{pro} (contours) for Case I. (b) Spatial distribution of NRD between A1_K and A4_K for L . Shaded areas are NRD > 1%.

YECS (14 m/s northwesterly winds) are applied to the circulation system, the spatial distribution of maximum V_{pro} is obtained (contours, in Fig. 6a). In this figure, the largest V_{pro} occurs along the Kuroshio, but the magnitude is small (<0.3 m/s). This may be because the current direction and the mean propagation direction of the waves are almost perpendicular. Consequently, the effect of oceanic circulation on mean wave parameters is relatively smaller than that of tides as seen in the NRD distribution (Fig. 6b) between A1_K and A4_K for L (the maximum is below 2.5%).

4.4. Combined effect of tides, storm surges and oceanic circulation

Combined effects of elevations and currents induced by tides, storm surges, and oceanic circulation on waves are analyzed in four numerical experiments, A1_A, A2_A, A3_A, and A4_A, for Case II. During a passage of Winnie, surface current fields were generated by taking into account realistic tides, storm surges, and oceanic circulation (arrows, in Fig. 7a). The maximum V_{pro} is obtained using the difference of direction between wind and wave (contours, in Fig. 7a). The distribution of maximum V_{pro} shows that the strongest following currents occur on the west coast of Korea, at the Yangtze River mouth, and along the track of Winnie. This strongly corresponds to that of the NRD for T_a (Fig. 7b). The strongest combined effects (the largest NRD) of all processes on T_a are found around the Yangtze River mouth where both tides and storm surges influence. At a station ‘B’ in this area (see Fig. 1), the simulated T_a and L are presented as a function of time in Fig. 8a and b. In these figures, the oscillation (in relative values from A4_A) of a tidal period (about 12 h), which is appeared in Fig. 8c and d, is found when the effect of elevation

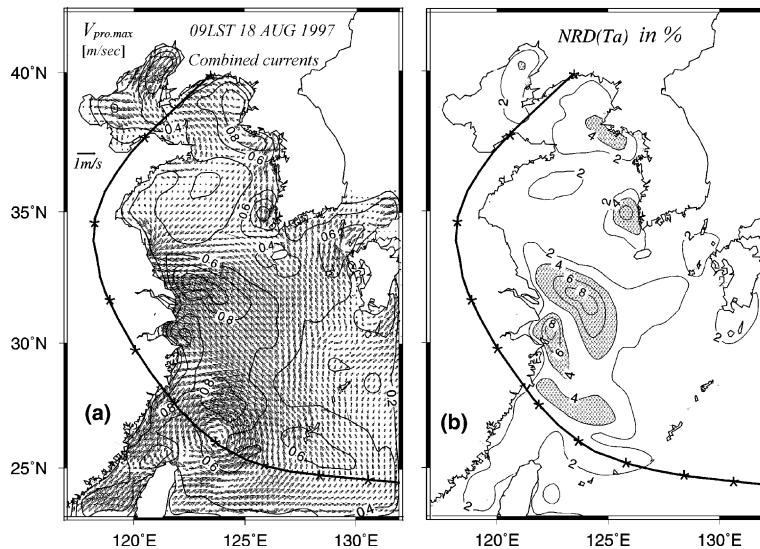


Fig. 7. (a) Spatial distribution of combined surface currents (arrows) considering tides, storm surges, and oceanic currents at 09h LST, 18 August 1997 and their maximum V_{pro} (contours) for Case II. (b) Spatial distribution of NRD between A1_A and A2_A for T_a during a passage of Winnie. Shaded areas are NRD $> 4\%$.

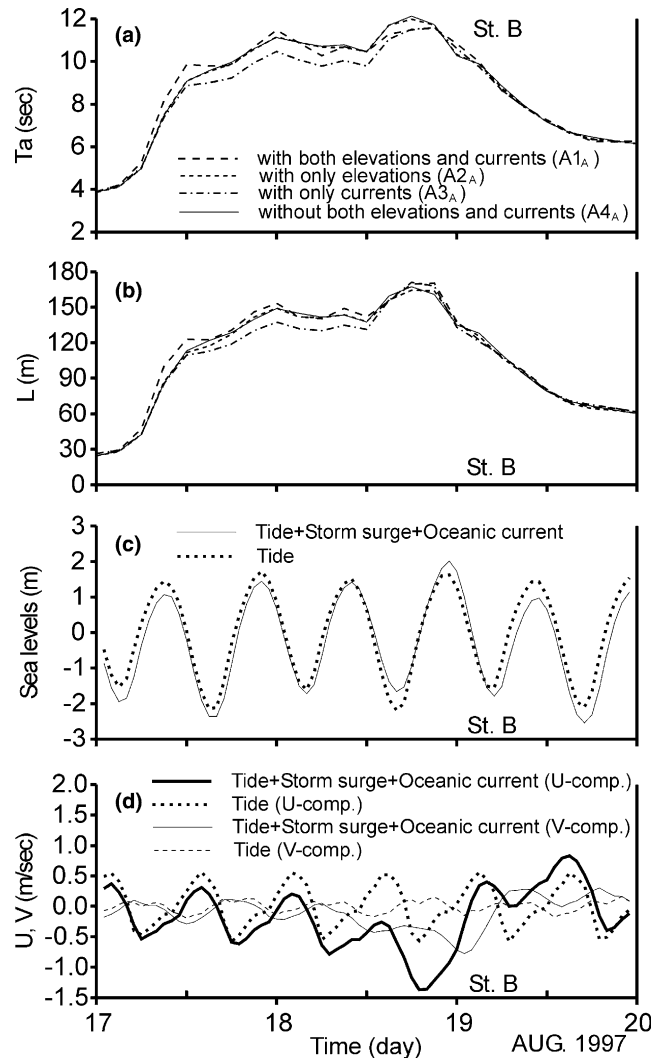


Fig. 8. (a,b) Time series of T_a and L simulated from four experiments (A1_A, A2_A, A3_A, and A4_A) for Case II at station 'B'. (c,d) Variations of sea levels and current components (U and V) during simulations. Solid lines represent the combined sea levels (or currents) and dotted lines represent the tide-induced sea levels (or currents).

is considered (i.e., in A1_A and A2_A), but not found when current effect is considered (i.e., in A3_A). This means that the effect of elevation at this location is tide-dominated, whereas that of current is surge-dominated. Although both elevation and current contribute to wave modulation, the combined effect of the modulation is tide-dominated since A1_A (dashed lines) considering total currents and elevations shows a clear tidal signal. During a passage of Winnie, the model results of H_s and T_a at Chilbado (Fig. 1) are compared with buoy observations in Fig. 9. This shows that the modulation of a tidal period is consistent with Fig. 8, in both observations and coupled model results especially in the wave period.

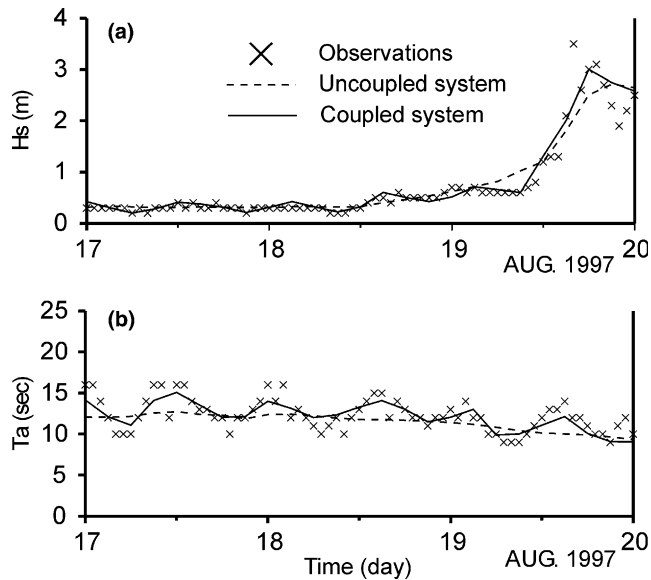


Fig. 9. Comparisons of simulated H_s and T_a with observations at Chilbaldo buoy. The results of coupled and uncoupled simulations are obtained from A1_A and A4_A for Case II, respectively.

5. Impact of the coupled system on coastal circulation and water-mass modeling

5.1. Effect of tides

Tides in the YECS account for the major part of overlying current. Most numerical studies (Yanagi and Takahashima, 1993; Jacobs et al., 2000) on the seasonal circulation of the YECS, however, have neglected tidal effect partly because there were difficulties in the use of open boundary condition with tides, and partly because there were assumptions that tidal motion with its short time scale had little influence on the oceanic circulation with a large time scale. In this section, we investigate how tides in the YECS affect seasonal circulation and water-mass simulations. For this purpose, we designed two experiments: B1 (monthly mean simulation considering wind, heat flux, river input and tides) and B2 (like B1, but without considering tides). In B1, eight tidal constituents were used to simulate the realistic tides and the results are presented after removing tides. In this experiment, POM is initialized with the output of a two-month spin-up in which POM is forced by February mean winds (Na and Seo, 1998), temperature, and salinity fields (Levitus and Boyer, 1994). The volume transport used in the open boundaries has been shown in Fig. 1. From this initialization, monthly mean prognostic simulation is performed during a one-year continuous calculation and then three-dimensional distributions of current, temperature, and salinity are obtained every month.

Fig. 10 shows the distributions of surface current in winter simulated by B1 and B2 and their differences in current direction and speed. The significant tide-induced changes in the current speed and direction are found along the East Coast of China and along the trough (deeper than 80 m) of the Yellow Sea. Especially, the surface current moving northwestward along the trough of the Yellow Sea becomes much weaker and their direction changes clockwise to 30–60°. Bottom

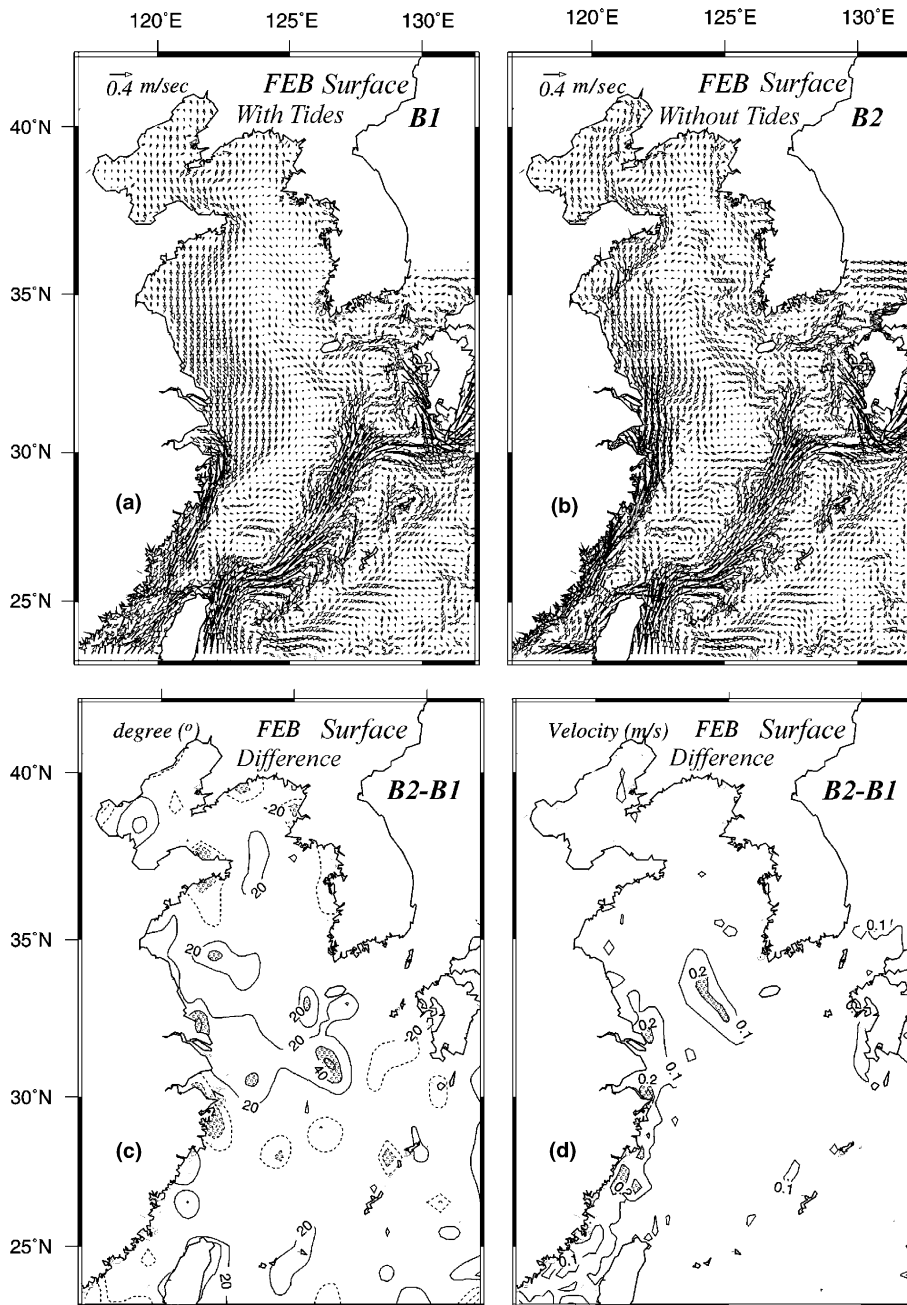


Fig. 10. (a,b) Spatial distributions of surface current on February simulated from the monthly mean calculation with considering tides (B1) and without considering tides (B2). (c,d) Differences between B2 and B1 in current directions and speeds. Shaded areas are where the differences are over 40° in directions and over 0.2 m/s in speeds.

current streak paths (Fig. 11a) also reveal a significant change of bottom current due to the tidal effect. The change of the current system can be explained by a nonlinear interaction between tides

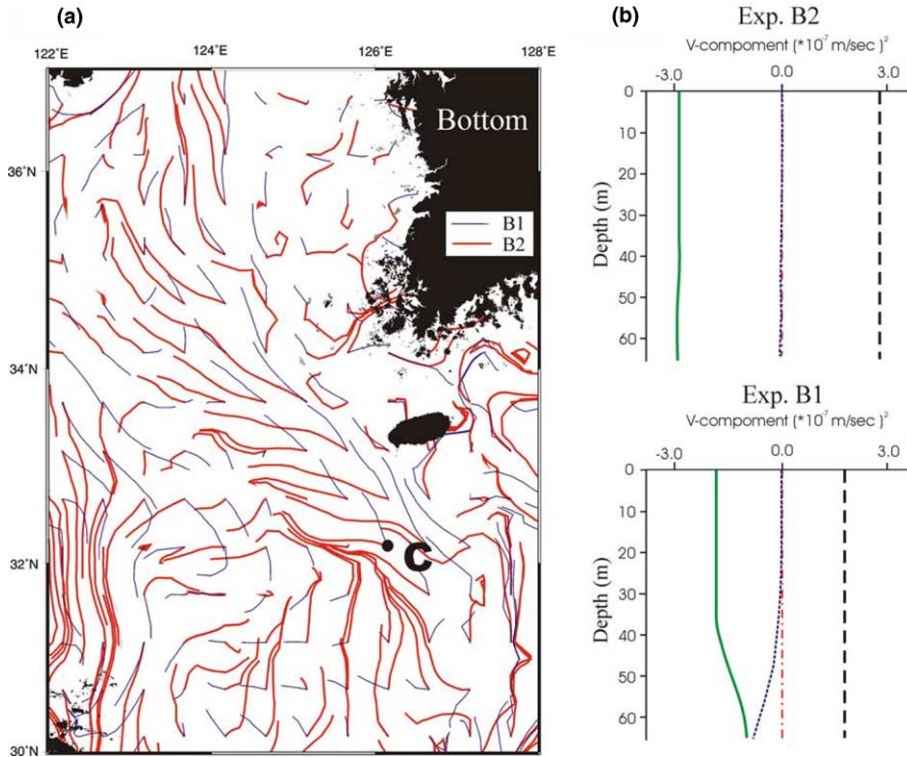


Fig. 11. (a) Bottom current streak paths of 28-day duration using 3-day average values on February (blue line: with tides, red line: without tides). (b) Comparison between B2 (upper panel) and B1 (lower panel) in the momentum balance profile (for V-component) at a point ‘C’ on February (pressure gradient is a dashed line; Coriolis force is a solid line; advection is a dash-dot line; vertical diffusion term is a dotted line).

and oceanic currents in a quadratic bottom friction term (Prandle and Wolf, 1978; Lee, 1999; Moon and Oh, 2003). For further understanding of its dynamics, we examine the momentum balance for two experiments throughout the total depth at a point ‘C’ of the southern side of Cheju (see Fig. 11a) where a significant change of current direction is shown. Fig. 11b shows that, in the case of B2 neglecting tides (upper panel), the advection effect is negligibly small and the resultant geostrophic balance between the pressure gradient and Coriolis force is predominant. However, in the case of B1 considering tides (lower panel), the vertical diffusion of momentum induced mainly by the quadratic bottom friction terms is no longer negligible. In this case, the pressure gradient term, especially near bottom, is balanced with the sum of the Coriolis force and the vertical diffusion terms. Therefore, if the advection and the horizontal diffusion of relative vorticity are neglected under the assumption that $\xi/h \ll 1$, the vorticity balance in a steady state is given as

$$\frac{\gamma}{h} U \cdot \nabla h = \hat{k} \cdot \nabla \times \left(\frac{\tau_b}{h} \right), \tag{21}$$

where ξ is the displacements at the surface, h is the mean water depth, U is the depth-averaged current vector, γ is the Coriolis parameter, τ_b is the bottom friction, and \hat{k} is the unit vector in

vertical direction (Lee, 1999). From this equation, we can obtain a simple equation, $U \cdot \nabla h \approx 0$, in B2 since the bottom friction in B2 goes nearly to zero as shown in the upper panel of Fig. 11b. In this case, the flow is characteristic of geostrophic flow and runs almost parallel with bottom topography. On the other hand, the effect of bottom friction in B1 is no longer negligible (as shown in the lower panel of Fig. 11b) and consequently the current direction tends to cross the isobaths, turning to the right rather than going straight into the center of the Yellow Sea. This explains the 30–60° clockwise change of winter current southwest of Chejudo. Because of these changes, sea surface temperatures along the trough of the Yellow Sea decrease by about 1–4 °C (Fig. 12a–c). Comparing contour lines of 8 and 14 °C between model simulations (Fig. 12a and b) and observation (Fig. 12d) shows that the inclusion of tides seems to prevent warm water with tongue-like shape penetrating into the trough of the Yellow Sea, leading to more realistic simulation of SST distribution.

Current distribution in summer is also affected by inclusion of tides significantly at the surface and bottom. Flows along the trough of the Yellow Sea and the west coast of Korea changed their directions significantly (Fig. 13c). Flows to the east or north associated with the Yangtze River are also weakened by tides up to 25 cm/s (Fig. 13d). The modulation of current in summer contributes to the change of three-dimensional temperature distribution in the YECS. At the sea surface, the temperature's change reaches up to about 1–3 °C (Fig. 14a–c). In summer, it is known that tidal fronts are formed in a boundary between well-mixed and stratified regions by the tidal mixing processes and are found along the Chinese coast between 30°N and 35°N, and along the west coast of Korea (Cho and Seung, 1989). The observed summer tidal fronts along the west coast of Korea are simulated successfully when tides are considered (compare Fig. 14d with Fig. 14a and b).

5.2. Effect of wind waves

In regions where strong vertical stratification exists, especially in summer, the strong wind stress generated by typhoons stirs the water mass to make water columns well mixed regionally. This affects not only SST but also three dimensional temperature distributions in a synoptic time scale. It is known that wind stress is affected by ocean waves significantly (Mastenbroek et al., 1993; Zhang and Li, 1996) and that breaking effects and Langmuir circulations caused by the ocean waves also play an important role in ocean mixing (Craig and Banner, 1994; Kantha and Clayson, 2004; Mellor and Blumberg, 2004). Ocean waves, therefore, may have a strong impact on ocean temperature distributions. In this section, the effects of ocean waves on coastal circulation and water-mass simulations are investigated focusing on the associated SST change during a passage of Winnie. For this purpose, four experiments for Case II are designed (see Table 1): C1 (coupled simulation with the wave-dependent stress), C2 (uncoupled simulation without wave effect), C3 (the same as C1, but with Langmuir circulations), C4 (the same as C1, but with both breaking waves and Langmuir circulations). In these experiments, the model is initialized using the analyzed RDAPS data of 12-h interval and the analyzed weekly SST data from the National Centers for Environmental Prediction (NCEP) for 7 days after the monthly mean prognostic calculation of August. Then the distributions of current and SST are finally simulated for a passage of Winnie using hourly wind and heat flux data obtained from the hurricane model of KMA.

Fig. 15 is a SST distribution simulated by C4 considering both tides and waves when Winnie approaches the East Coast of China (12h LST 18 August 1997). In the figure, typhoon-induced

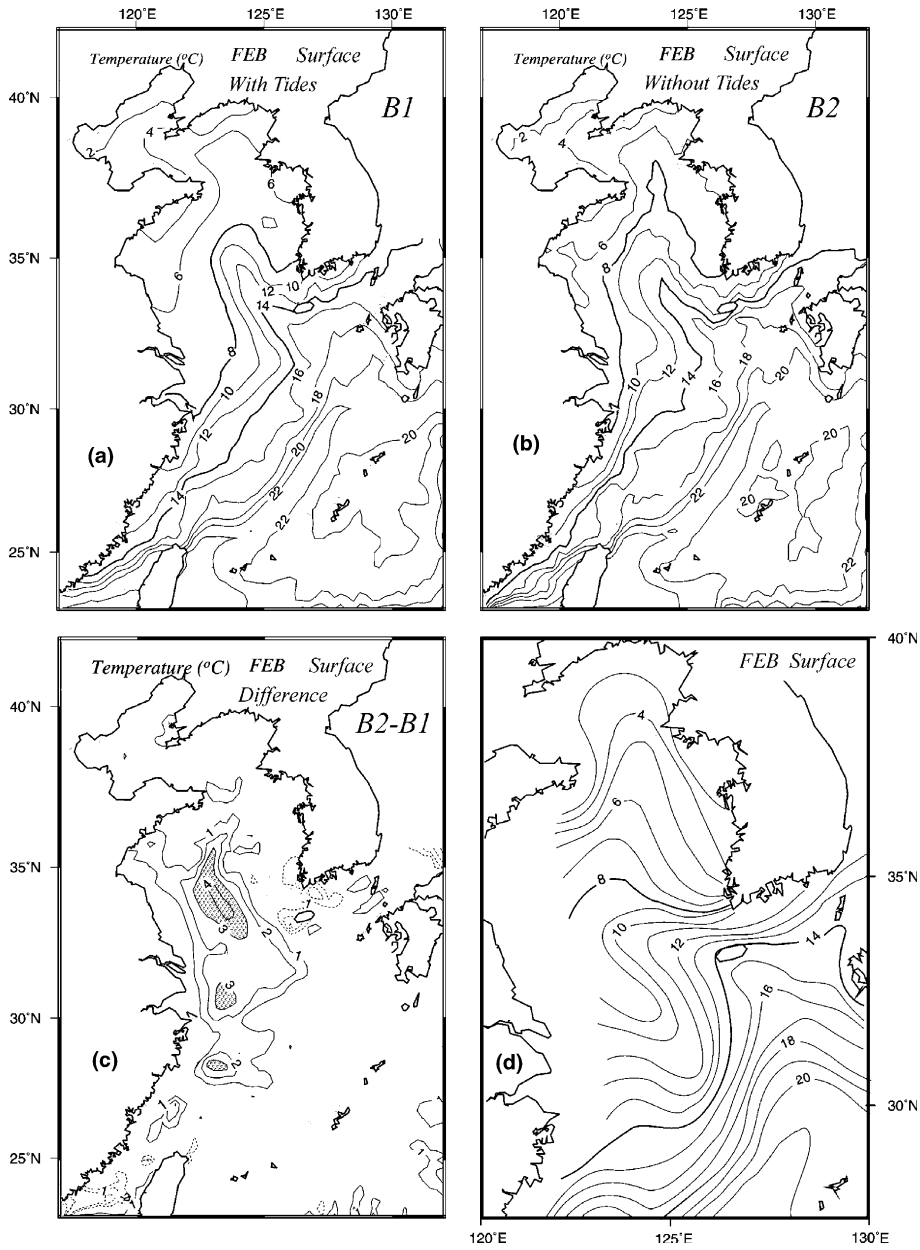


Fig. 12. (a,b) SST distributions for February simulated from the monthly mean calculation with considering tides (B1) and without considering tides (B2). (c) SST differences between B2 and B1. Shaded areas are where the differences are over 3 °C. (d) The observed monthly mean SST distribution of February based on the Japan Oceanography Data Center (JODC) data (Lee, 1996).

strong currents and turbulences deepen the ocean mixed layer and lead to a SST decrease of up to 3.8 °C along the storm track (compare Fig. 15 with Fig. 14a). It is known that SST decrease

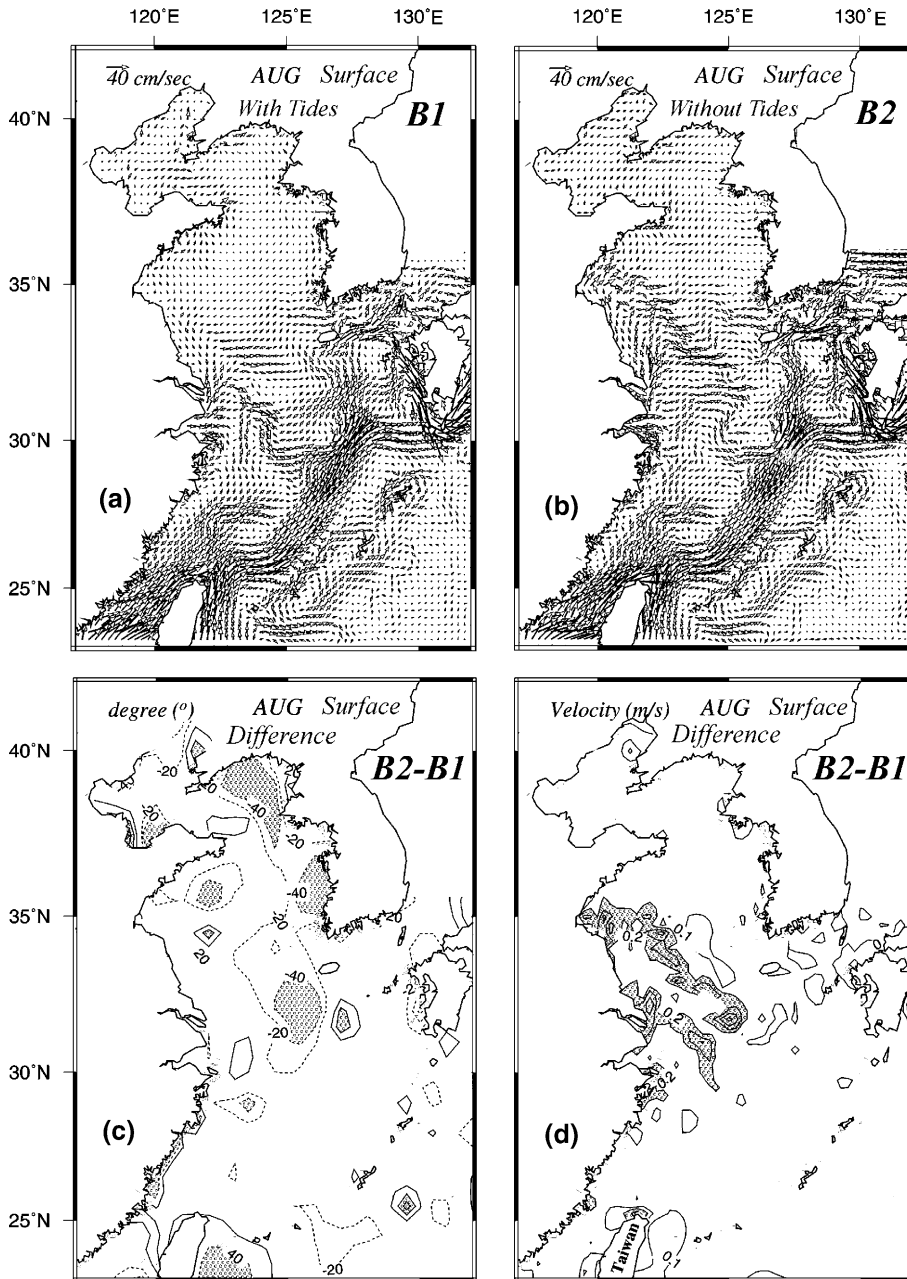


Fig. 13. Same format as in Fig. 10, but for August.

induced by tropical cyclones has been observed to vary 1–6 °C (Black, 1983). The magnitude of the SST variation is determined mostly by storm translation speed (Bender et al., 1993). Winnie was moving with the storm translation speed of 4–6 m/s before landing. The SST decrease estimated by the present model is consistent with that obtained by Bender et al. (1993) from various

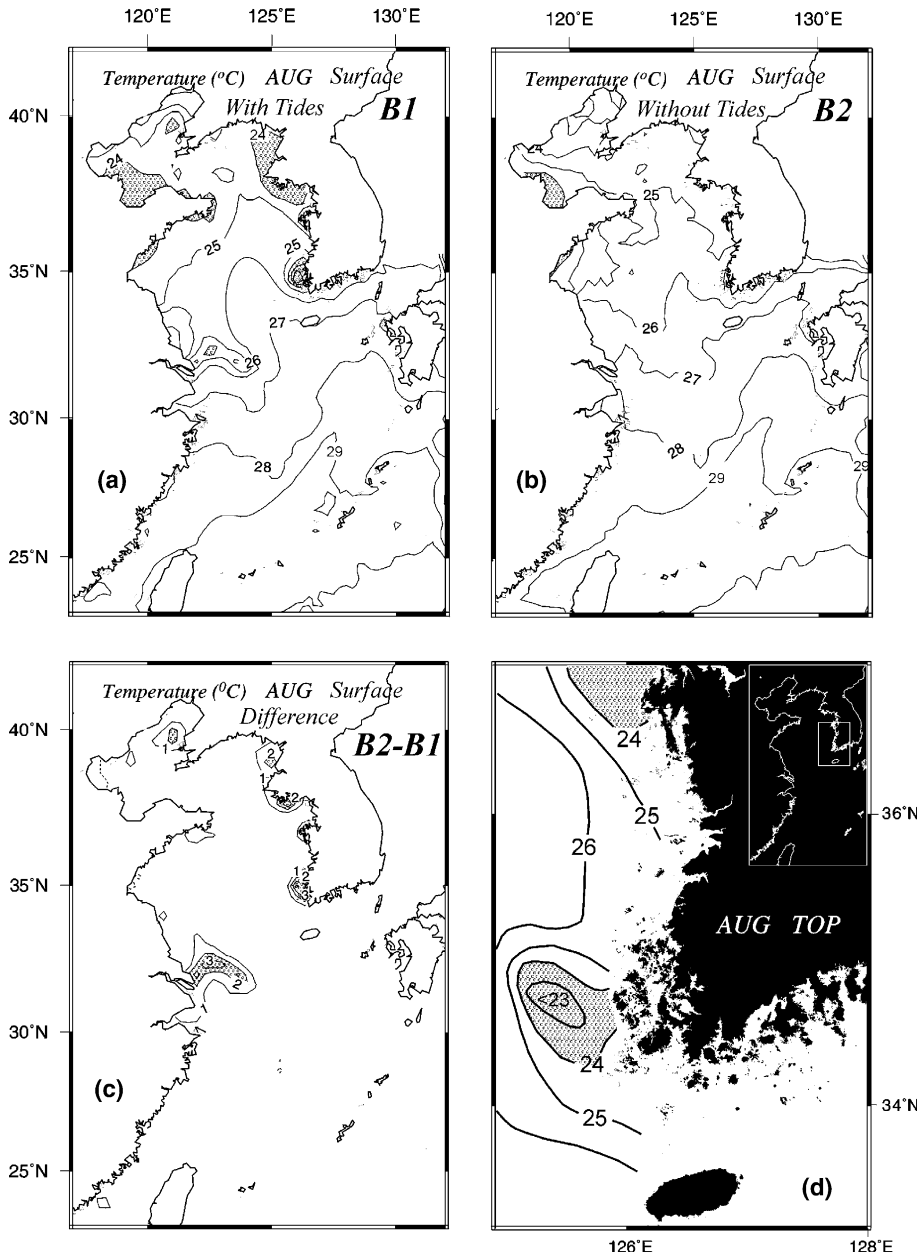


Fig. 14. Same format as in Fig. 12, but for August. The observed monthly mean SST distribution of August is based on KORDI (1987). Shaded areas are where the temperatures are below 24 °C or the differences (B2–B1) are over 2 °C.

hurricanes of similar speed. This amount of SST decrease underneath the typhoon can significantly reduce the heat and moisture fluxes at the sea surface, which may play an important role in storm evolution (Bender and Ginis, 2000).

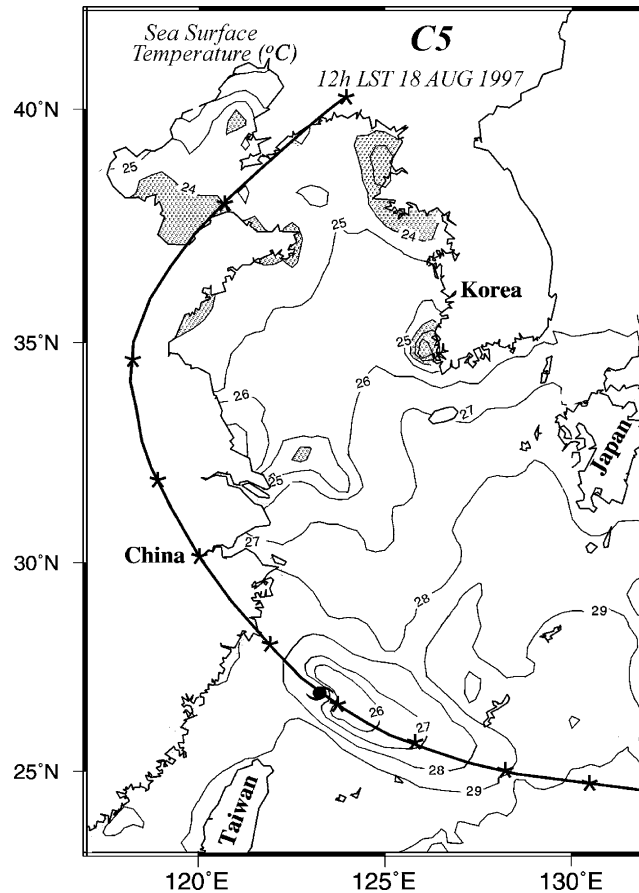


Fig. 15. SST distributions at 12h LST 18 August 1997 simulated from the coupled simulation (C1). Shaded areas are where the temperatures are below 24 °C.

In order to quantify the contribution of surface waves to the SST changes the simulated SSTs for four experiments (C1–C4) are presented as a function of time at station ‘B’ located at Winnie’s track (Fig. 16). The figure show that the SST is not really affected by the inclusion of Langmuir terms, but significantly effected by the inclusion of wave breaking and wave-dependent stress. It is known that wave breaking has an important impact on TKE and its dissipation rate near the sea surface, but the highly dissipative nature of turbulence makes the TKE injected at the surface by wave breaking decay rapidly with depth, resulting in typically confining the effect to the upper few meters (Kantha and Clayson, 2004). Therefore, in the present summertime simulations when the surface layer is relatively shallow, the wave breaking effect can be expected to be significant. At station ‘B’, the maximum temperature drop due to the wave breaking is about 0.5 °C. On the other hand, the small contribution of Langmuir circulation to the present SST changes seems to be caused by the exclusion of Langmuir turbulence in the TKE equation. Inject of turbulence into the mixed layer from Langmuir circulation, which is not considered in the present study, may play a more significant role in ocean mixing and corresponding SST distributions.

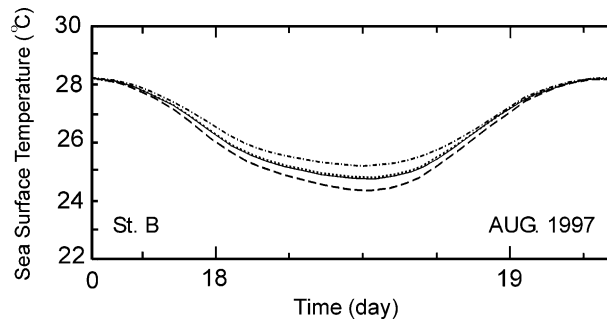


Fig. 16. SST variations simulated from four experiments (C1–C4) for Case II at station ‘B’. A dotted line represents C1 considering wave-dependent surface stress; a dot-dashed line represents C2 without any wave effects; a solid line represents C3 including Langmuir terms and wave-dependent stress; a dashed line represents C4 considering Langmuir terms, wave-dependent stress, and wave breaking effects.

The impact of wave-dependent stress on the SST changes is as significant as wave breaking. It causes a decrease of up to 0.5 °C during the Winnie event. This is explained by comparisons of spatial distributions estimated by wave-dependent stress and traditional wind-dependent stress under typhoon wind forcing. When Winnie approaches the shore, C_d based on the wind-dependent stress expression of Wu (1982) shows symmetric distribution similar to wind as expected (Fig. 17a and b), while the distributions of ocean wave and corresponding wave-dependent C_d show a large spatial variability around the storm (Fig. 17c and d). Fig. 17c shows distributions of the significant wave height H_s (contours), mean wave direction (arrows), and mean wavelength L (arrow length) estimated from the coupled model. An area with oblique lines indicates that the wave age (c_p/u_*), which is defined as the phase velocity (c_p) of the peak frequency divided by the friction velocity (u_*), is less than 10 (i.e., an area with very young waves). This shows that waves are generally higher, longer, and more developed in the front right quadrant of the storm track and lower, shorter, and younger in the rear left quadrant, despite the relative symmetry of the wind speed. This is because waves to the right front quadrant of the storm track are exposed to prolonged forcing from wind while waves to the left rear quadrant are exposed to the decreased effective fetch and duration from wind forcing due to storm motion (Moon et al., 2003a). By considering these wave fields, the associated distribution of C_d is asymmetric about the center of storm vortex (Fig. 17d). The drag is, in general, larger in the rear left quadrant and smaller in the front right quadrant, implying that the present model predicts higher drag with younger waves.

Fig. 18 is a scatterplot of the non-dimensional roughness length, i.e., Charnock coefficient ($z_{Ch} = z_0 g / u_*^2$) as a function of wave age in all grid points during the Winnie event. Solid line represents the HEXOS parameterization, $z_{Ch} = 0.48(c_p/u_*)^{-1}$ (Smith et al., 1992), which gives values that are consistent with both observations in the open ocean (Smith, 1980) and in Lake Ontario (Donelan, 1990). In general, our results show a good agreement with the HEXOS fit where z_{Ch} decreases with wave ages. Our clear dependency of z_{Ch} on wave ages is consistent with results of other field observations (Oost et al., 2001; Drennan et al., 2003). The large scatter in Fig. 18 may be caused by the existence of swell that is mostly experienced by hurricane condition or the topography effect due to shoaling and bottom friction in shallow areas (Komen et al., 1998).

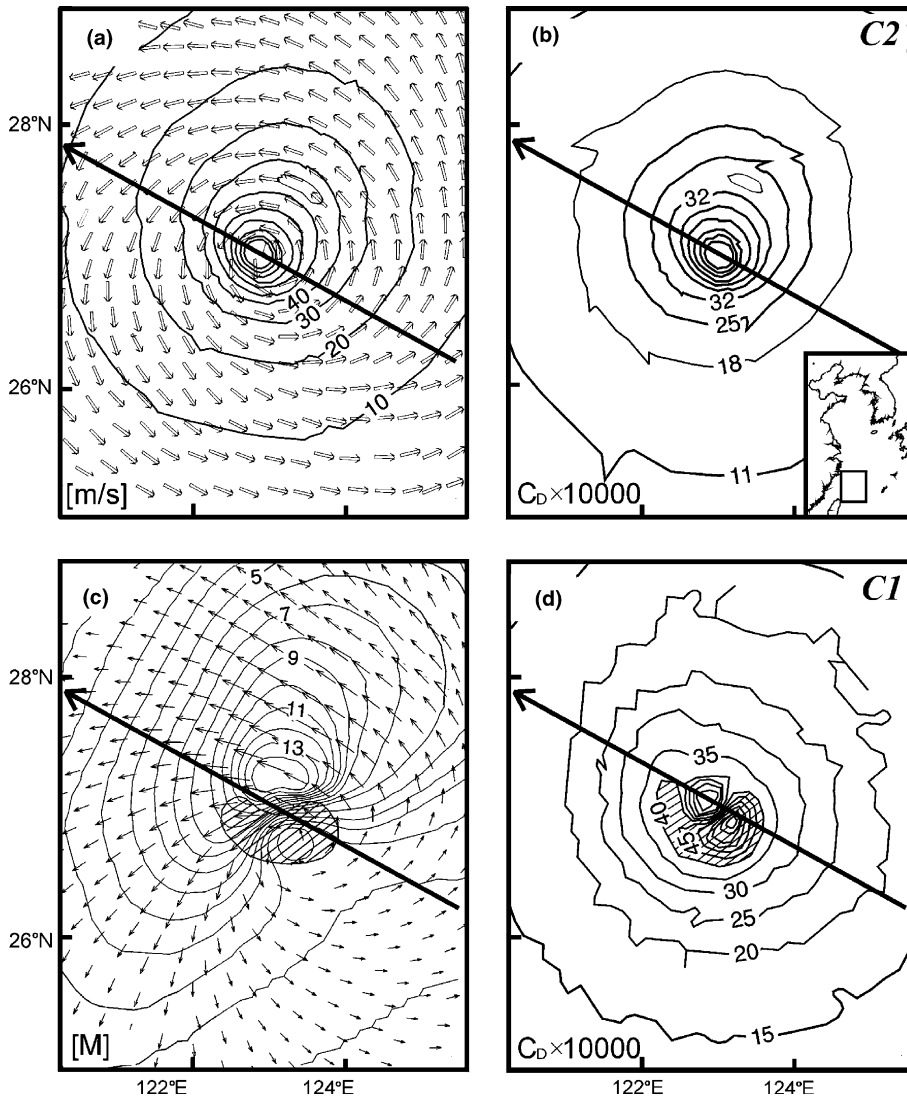


Fig. 17. (a) Wind fields at 12h LST 18 August 1997 (wind speed: contours, wind directions: thin arrows, storm track: a thick arrow). (b) Distribution of C_d estimated from Wu's drag relationship (C2). (c) The simulated wave fields at 12h LST 18 August 1997 (significant wave heights: contours, mean wave directions: arrows, mean wavelength: arrow length, shaded area: wave age is less than 10). (d) Spatial distribution of C_d estimated using wave-dependent stress (C1) (shaded area is $C_d > 4 \times 10^{-3}$).

Although our general pattern of z_{Ch} is dependent on wave age, a closer examination of Fig. 18 shows that a maximum z_{Ch} seems to occur at wave ages of about $c_p/u_* = 6$ and z_{Ch} tends to increase with wave ages for $c_p/u_* < 6$, although the scatter is large and the trend is not very clear. In previous studies, Komen et al. (1998) indicated a clear increase of z_{Ch} with wave ages for $c_p/u_* < 5$ from idealized simulation for duration-limited growth with WAM model. Johnson et al. (1999) also reported the similar results using WAM model in restricted fetch areas, but it was not so

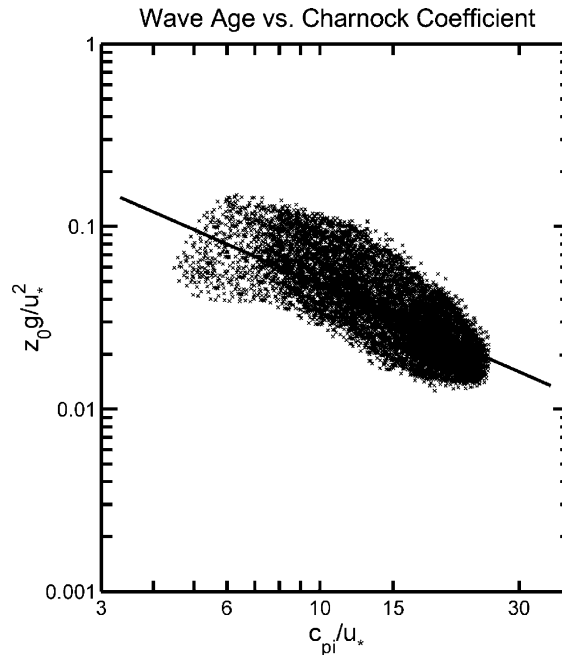


Fig. 18. Scatterplots of z_{Ch} as a function of wave ages in all grid points during the Winnie event. Solid line represents the HEXOS parameterization (Smith et al., 1992).

evident due to insufficient data in very young waves. Recently, Moon et al. (2004a,b) showed a similar tendency using a wave boundary model and WAVEWATCH III (Tolman, 2002) model, but this behavior was only found in very strong wind speeds (>35 m/s).

For the extreme young waves with short duration (or fetch), we can predict that z_{Ch} is low simply because there are not enough waves to carry the stress. This is straightforward when we considering that the roughness at the initial wave stage (very young waves) after the onset of wind increases gradually from zero with time. This explains why z_{Ch} in extreme young wind seas ($c_p/u_* < 6$) encountered by hurricane condition is leveling off or even decreasing as seen in Fig. 18. It should be noticed, however, that such extreme young seas are only found at very high winds in reality since they do not last long at moderate wind. Most observations so far are from less than 30 m/s (Jones and Toba, 2001). This can explain why the trend (younger seas produce less z_{Ch}) was not found in most field observation studies.

6. Summary and conclusion

A coupled ocean wave–tide–circulation system has been developed and applied to numerical experiments involving wind waves, coastal circulation, and water-mass simulations in the Yellow and East China Seas (YECS). The coupled system is based on the synchronous two-way coupling of a third-generation wave model, WAVEWATCH-II and a three-dimensional Princeton Ocean Model, POM. In the coupling scheme, WAVEWATCH-II calculates the sea surface stress, wave

breaking effect, Stokes drift and gives them to the ocean model. POM calculates current and elevation and gives them to the wave model. Using this coupled system, the present study aims to investigate the effect of ocean waves and tides on coastal circulation and water-mass modeling and the effect of tides, storm surges, and coastal circulation on wind wave modeling. This may be the first two-way coupling study of a surface wave model and an ocean model taking into account major physical processes in coastal region, such as realistic tides, wind waves, storm surges, oceanic circulations, surface heat flux, fresh water input, and all their interactions.

From experiments using the coupled system, it is found that wind waves are influenced by both currents and sea level elevation induced by tides, storm surges, and oceanic circulation. Tides are the most influential factor in modulating mean wave characteristics in the YECS. Typical magnitudes of the modulation are 4–12%. For absolute periods, the wave–tide interactions are induced mainly by local tidal currents, whereas those for wave height and wave length are caused by local water depth. The tide-induced modulations of the mean wave parameter are found to decrease with increasing severity of winds, and the magnitude of the modulation at neap tides is found to be half that at spring tides. The effect of storm surge and oceanic circulation on wind waves is found to be less distinct than that of tides with an overall effect below 3%.

On three-dimensional coastal circulation and water-mass structures in the YECS, tides significantly affect seasonal circulation patterns of the YECS. When tides are included in the winter simulation, the most significant changes are found in northwestward surface currents along the trough of the Yellow Sea where currents become much weaker and their direction changes clockwise to 30–60° due to tide-increased bottom friction. This leads to a change of up to 4 °C in temperatures at the surface and bottom along the trough of the Yellow Sea. In summer, observed tidal fronts on the west coast of Korea are simulated successfully when tides are considered. Tidal mixing decreases surface temperature up to 3 °C in strong tidal areas. From these results, we can conclude that ocean circulation and water-mass modeling in the YECS that does not consider realistic tides may lead to inaccurate results.

The effect of ocean waves on coastal circulation and SST simulation is investigated considering wave-dependent stress, wave breaking parameterization, and Langmuir circulation during typhoon Winnie's passage. The coupled simulation with these wave effects shows that typhoon-induced strong currents deepen the ocean mixed layer and lead to a SST decrease of up to 3.8 °C along the storm track. Sensitivity experiments indicate that the SST is affected by inclusion of wave breaking and wave-dependent stress, but not much influenced by the inclusion of Langmuir terms. It seems that wave breaking has an important impact on TKE and its dissipation rate near the sea surface, resulting in a significant SST change (drop of maximum 0.5 °C). Langmuir circulations have little effect on the SST change (<0.08 °C) because the present model excludes Langmuir turbulence effects in the TKE equation, which may play a more significant role in ocean mixing. The impact of wave-dependent stress on the SST seems to be produced by a significant enhancement of stress around storm center as well as a large variability of stress fields in space and time. The coupled simulation indicates that higher, longer and more developed waves in the right front quadrant of the storm track produce smaller sea drag; lower, shorter and younger waves to the rear left quadrant produce larger sea drag, despite the relative symmetry of wind speed. Although this behavior, (i.e., the drag or non-dimensional roughness z_{Ch} decreases with wave age), is dominant in a scatterplot of z_{Ch} against wave age, z_{Ch} tends to have a maximum about $c_p/u_* = 6$ and then to increase with wave ages for $c_p/u_* < 6$. This result suggests that the extreme young seas

do not produce higher drag, simply because there are not enough waves to carry the stress in such short-duration (or -fetch) circumstances. It should be noticed that such young waves, in reality, are only observable in very fast-moving storms with very strong winds. This can explain why the trend (younger seas produce less z_{Ch}) was not found in most field observation studies.

The present results suggest that accurate ocean and atmospheric modeling requires the coupling of a surface wave model capable of predicting wave and stress fields varying in time and space. This is because wind stress is strongly dependent on surface-wave fields. Under typhoon conditions, ocean waves consist of many swells propagating at large and sometimes conflicting angles to the local wind (Moon et al., 2003a), which may influence both the magnitude of wind stress and the angle difference between wind stress and mean wind (Grachev et al., 2003). Therefore, wind stress needs to be treated as a vector quantity in the complex seas.

As predicted by Zhang and Li (1997), Welsh et al. (2000), Bao et al. (2000), Kantha and Clayson (2004), and Mellor (2003a), more processes than used here are related to the coupling of ocean circulation model and surface wave model such as the wave-induced stress bottom stress, the effect of sea spray on surface fluxes, the influence of Langmuir turbulence on the upper ocean mixing, the inclusion of radiation stress in momentum equation, and wave's effect in mass flux. In momentum transfer from atmosphere to ocean current, surface stress also should be corrected because waves retain momentum, which is spent in growth or advected away. We expect that the inclusion of these effects in the present model will lead to more realistic simulations in coastal areas. This will be the subject of our next investigation. It is important to realize, however, that estimating these effects quantitatively is very difficult because of imperfect knowledge of the processes. Although the present coupled system is not complete because it neglects above processes, we believe that this study, as an important step toward a fully coupled wave–circulation modeling, provides an improved simulation for wind waves, tides, storm surges, circulation, and water-mass distributions in coastal areas using important coupling processes as well as a plausible explanation of how waves, tides, and circulation influence each other.

Acknowledgements

The author gratefully thanks Professor Im Sang Oh at Seoul National University for his advice, encouragement, and support. The author also thanks Dr. Hendrik Tolman at NOAA/NCEP Environmental Modeling Center for his assistance in making a coupled model. Professor George L. Mellor at Princeton University is also thanked for his helpful review and comments. The author acknowledges the support of oceanic and atmospheric data from the Korea Meteorological Administration, the Meteorological Research Institute, the Korean Ocean Research and Development Institute, and the National Oceanographic Research Institute. The author also acknowledges two anonymous reviewers for their helpful comments.

References

- Bao, J.-W., Wilczak, J.M., Choi, J.-K., Kantha, L.H., 2000. Numerical simulations of air–sea interaction under high wind conditions using a coupled model: a study of hurricane development. *Mon. Weather Rev.* 128, 2190–2210.

- Bender, M., Ginis, I., 2000. Real-time simulations of hurricane-ocean interaction using a high-resolution coupled model: effects on hurricane intensity. *Mon. Weather Rev.* 128, 917–946.
- Bender, M.A., Ross, R.J., Tuleya, R.E., Kurihara, Y., 1993. Improvements in tropical cyclone track forecasts using the GFDL initialization system. *Mon. Weather Rev.* 121, 2046–2061.
- Black, P.G., 1983. Ocean temperature changes induced by tropical cyclones. Ph.D. Dissertation, The Pennsylvania State University, 278 pp.
- Blumberg, A.F., Mellor, G.L., 1987. A description of a three-dimensional coastal ocean circulation model, three-dimensional coastal ocean models. In: Heaps, N. (Ed.), *Three-dimensional Coastal Ocean Models*, vol. 4. Amer. Geophys. Union, pp. 1–16.
- Bretherton, F.P., Garrett, C.J.R., 1968. Wave trains in inhomogeneous moving media. *Proc. R. Soc. London, A* 302, 529–554.
- Cavaleri, L., Rizzoli, P.M., 1981. Wind wave prediction in shallow water: theory and applications. *J. Geophys. Res.* 86, 10961–10973.
- Cho, C.H., Seung, Y.H., 1989. An oceanographic survey of tidal front around Kyunggi Bay. *Yellow Sea Res.* 2, 51–61.
- Choi, B.H., Eum, H.M., Woo, S.B., 2003. Modeling of coupled tide–wave–surge process in the Yellow Sea. *Ocean Eng.* 30, 739–759.
- Craig, P.D., Banner, M.L., 1994. Modeling wave-enhanced turbulence in the ocean surface layer. *J. Phys. Oceanogr.* 24, 2546–2559.
- Craik, A.D.D., Leibovich, S., 1976. A rational model for Langmuir circulation. *J. Fluid Mech.* 73, 401–426.
- Davies, A.M., Lawrence, J., 1995. Modeling the effect of wave–current interaction on the three-dimensional wind-driven circulation of the eastern Irish Sea. *J. Phys. Oceanogr.* 25, 29–45.
- Donelan, M.A., 1990. Air–sea interaction. In: LeMehaute, B., Hanes, D.M. (Eds.), *The Sea*. John Wiley and Sons, pp. 239–292.
- Drennan, W.M., Kahma, K.K., Terray, E.A., Donelan, M.A., Kitaigorodskii, S.A., 1992. Observations of the enhancement of kinetic energy dissipation beneath breaking waves. In: Bannerand, M.L., Grimshaw, R.H.J. (Eds.), *Breaking Waves*. Springer, pp. 95–101.
- Drennan, W.M., Donelan, M.A., Terray, E.A., Katsaros, K.B., 1996. Oceanic turbulence dissipation measurements in SWADE. *J. Phys. Oceanogr.* 28, 1624–1641.
- Drennan, W.M., Graber, G.C., Hauser, D., Quentin, C., 2003. On the wave age dependence of wind stress over pure wind seas. *J. Geophys. Res.* 108 (C3), 8062, doi: [10.1029/2000JC000715](https://doi.org/10.1029/2000JC000715).
- Edinger, J.E., Bradly, D.K., Geyer, J.C., 1974. Heat exchange and transport in the environment. Report No. 14, The Johns Hopkins University, Electric Power Research Institute Publication, No. 74-049-00-3, 125 pp.
- Flather, R.A., 1976. A tidal model of the northwest European continental shelf. *Mem. Soc. R. Sci. Liege* 10 (Ser. 6), 141–164.
- Gargett, A.E., 1989. Ocean turbulence. *Ann. Rev. Fluid Mech.* 21, 419–451.
- Grachev, A.A., Fairall, C.W., Hare, J.E., Edson, J.B., 2003. Wind stress vector over ocean waves. *J. Phys. Oceanogr.* 33, 2408–2429.
- Hasselmann, S., Hasselmann, K., 1985. Computations and parameterizations of the nonlinear energy transfer in a gravity-wave spectrum. Part I: A new method for efficient computations of the exact nonlinear transfer integral. *J. Phys. Oceanogr.* 15, 1369–1377.
- Hasselmann, K., Barnett, T.P., Bouws, E., Carlson, H., Cartwright, D.E., Enke, K., Ewing, J.A., Gienapp, H., Hasselmann, D.E., Kruseman, P., Meerburg, A., Müller, P., Olbers, D.J., Richter, K., Sell, W., Walen, H., 1973. Measurements of wind-wave growth and swell decay during the Joint North Sea Wave Project (JONSWAP). *Ergänzung. Deutsch. Hydrograph. Z.* 12, 95.
- Holthuijsen, L.H., Tolman, H.L., 1991. Effects of the Gulf Stream in ocean waves. *J. Geophys. Res.* C 96, 12755–12771.
- Jacobs, G.A., Hur, H.B., Riedlinger, S.K., 2000. Yellow and East China Seas response to winds and currents. *J. Geophys. Res.* 105 (C9), 21947–21968.
- Janssen, P.A.E.M., 1989. Wave induced stress and the drag of air flow over sea waves. *J. Phys. Oceanogr.* 19, 745–754.
- Janssen, P.A.E.M., 1991. Quasi-linear theory of wind-wave generation applied to wave forecasting. *J. Phys. Oceanogr.* 21, 1631–1642.

- Janssen, P.A.E.M., 1992. Experimental evidence of the effect of surface waves on the airflow. *J. Phys. Oceanogr.* 22, 1600–1604.
- Johnson, H.K., Vested, H.J., Hersbach, H., Højstrup, J., Larsen, S.E., 1999. The coupling between wind and waves in the WAM model. *J. Atmos. Oceanic Tech.* 16, 1780–1790.
- Jones, I.S.F., Toba, Y., 2001. *Wind Stress Over the Ocean*. Cambridge University Press. 303 pp.
- Kantha, L.H., Clayson, C.A., 2004. On the effect of surface gravity waves on mixing in the oceanic mixed layer. *Ocean Modell.* 6 (2), 101–124.
- Komen, G.J., Cavaleri, L., Donelan, M., Hasselmann, K., Hasselmann, S., Janssen, P.A.E.M., 1994. *Dynamics and Modeling of Ocean Waves*. Cambridge University Press. 520 pp.
- Komen, G.J., Janssen, P.A.E.M., Makin, V., Oost, W., 1998. On the sea state dependence of the Charnock parameter. *Global Atmos. Ocean Sys.* 5, 367–388.
- KORDI, 1987. *Oceanographic Atlas of Korean Waters, vol. 1, Yellow Sea*. KORDI. 147 pp.
- Lee, H.-C., 1996. A numerical simulation for the water masses and circulations of the Yellow Sea and the East China Sea. Ph.D. Thesis, Kyushu University, 150 pp.
- Lee, H.J., 1999. A three-dimensional mixed finite-difference Galerkin function model for the oceanic circulation in the Yellow Sea and the East China Sea. Ph.D. Thesis, Seoul National University, 141 pp.
- Levitus, S., 1982. *Climatological atlas of the world oceans*. NOAA Pro. Pap. 13, US Government Printing Office, Washington, DC, 103 pp.
- Levitus, S., Boyer, T.P., 1994. *World Ocean Atlas 1994, vol. 4, Temperature*. NOAA Atlas NESDIS 4, 129 pp.
- Longuet-Higgins, M.S., Stewart, R.W., 1960. Changes in the form of short gravity waves on long waves and tidal currents. *J. Fluid Mech.* 8, 565–583.
- Mastenbroek, C., Burgers, G., Janssen, P.A.E.M., 1993. The Dynamical coupling of a wave model and a storm surge model through the atmospheric boundary layer. *J. Phys. Oceanogr.* 23, 1856–1866.
- McWilliam, J.C., Sullivan, P.P., Moeng, C.-H., 1997. Langmuir turbulence in the ocean. *J. Fluid Mech.* 334, 1–30.
- Mellor, G.L., 2003a. The three-dimensional current and surface wave equations. *J. Phys. Oceanogr.* 33, 1978–1989.
- Mellor, G.L., 2003b. Users guide for a three-dimensional, primitive equation, numerical ocean model (June 2003 version). In: *Prog. in Atmos. and Ocean. Sci.*, Princeton University, 53 pp.
- Mellor, G.L., Blumberg, A., 2004. Wave breaking and ocean surface thermal response. *J. Phys. Oceanogr.* 34, 693–698.
- Mellor, G.L., Yamada, T., 1982. Development of a turbulence closure model for geophysical fluid problems. *Rev. Geophys. Space Phys.* 20 (4), 851–875.
- Moon, I.-J., 2000. Development of a coupled ocean wave–circulation model and its applications to numerical experiments for wind waves, storm surges and ocean circulation of the Yellow and East China Seas. Ph.D. Thesis, Seoul National University, Seoul, 213 pp.
- Moon, I.-J., Oh, I.S., 2003. A study of the effect of waves and tides on storm surge using a coupled ocean wave–circulation model. *J. Korean Meteorol. Soc.* 39 (5), 563–574.
- Moon, I.-J., Oh, I.S., Youn, Y.-H., 2000. A numerical study on the real-time sea level prediction along the western coast of Korea. *J. Korean Meteorol. Soc.* 36 (2), 203–218.
- Moon, I.-J., Ginis, I., Hara, T., Tolman, H., Wright, C.W., Walsh, E.J., 2003a. Numerical simulation of sea-surface directional wave spectra under hurricane wind forcing. *J. Phys. Oceanogr.* 33, 1680–1706.
- Moon, I.-J., Oh, I.S., Murty, T., Youn, Y.-H., 2003b. Causes of unusual coastal flooding generated by Typhoon Winnie on the west coast of Korea. *Nat. Hazards* 29, 485–500.
- Moon, I.-J., Hara, T., Ginis, I., Belcher, S.E., Tolman, H., 2004a. Effect of surface waves on air–sea momentum exchange: I. Effect of mature and growing seas. *J. Atmos. Sci.*, accepted for publication.
- Moon, I.-J., Ginis, I., Hara, T., 2004b. Effect of surface waves on air–sea momentum exchange: II. Behavior of drag coefficient under tropical cyclones. *J. Atmos. Sci.*, accepted for publication.
- Na, J.Y., Seo, J.W., 1998. The sea surface winds and heat fluxes in the East Asian marginal seas. 53 pp.
- Oh, I.S., Kim, Y.Y., 1992. Wave characteristics changes under a strong tidal current influence. *La mer* 30, 275–285.
- Oost, W., Komen, G.J., Jacobs, C.M.J., van Oort, C., Bonekamp, H., 2001. Indications for a wave dependent Charnock parameter from measurements during ASGAMAGE. *Geophys. Res. Lett.* 28 (14), 2795–2797.
- Prandle, D., Wolf, J., 1978. The interaction of surge and tide in the North Sea and River Thames. *Geophys. J. R. Astron. Soc.* 55, 203–216.

- Schiller, A., 2004. Effect of explicit tidal forcing in an OGCM on the water-mass structure and circulation in the Indonesian through flow region. *Ocean Modell.* 6, 31–49.
- Simmons, H.L., Jayne, S.R., St Laurent, L.C., Weaver, A.J., 2004. Tidally driven mixing in a numerical model of the ocean general circulation. *Ocean Modell.* 6 (3–4), 245–263.
- Smith, S.D., 1980. Wind stress and heat flux over the ocean in gale force winds. *J. Phys. Oceanogr.* 10, 709–726.
- Smith, S.D., Anderson, R.J., Oost, W.A., Kraan, C., Maat, N., DeCosmo, J., Katsaros, K.B., Davidson, K.L., Bumke, K., Hasse, L., Chadwick, H.M., 1992. Sea surface wind stress and drag coefficients: the HEXOS results. *Bound. Layer Meteor.* 60, 109–142.
- Tang, Y.M., Grimshaw, R., Sanderson, B., Holland, G., 1996. A numerical study of storm surges and tide, with application to the north Queensland coast. *J. Phys. Oceanogr.* 26, 2700–2711.
- Terray, E.A., Donelan, M.A., Agarwal, Y.C., Drennan, W.M., Kahma, K.K., Williams III, A.J., Hwang, P.A., Kitaigorodskii, S.A., 1996. Estimate of kinetic energy dissipation under breaking waves. *J. Phys. Oceanogr.* 26, 792–807.
- Tolman, H.L., 1989. The numerical model WAVEWATCH: a third generation model for the hind casting of wind waves on tides in shelf seas. *Communications on Hydraulic and Geotechnical Engineering*, Delft University of Technology, ISSN 0169-6548, Rep. No. 89-2.
- Tolman, H.L., 1990. The influence of unsteady, depths and currents of tides on wind-wave propagation in shelf seas. *J. Phys. Oceanogr.* 20, 1166–1174.
- Tolman, H.L., 1991. A third generation model for wind waves on slowly varying, unsteady, and inhomogeneous depth and currents. *J. Phys. Oceanogr.* 21, 782–797.
- Tolman, H.L., 2002. Validation of WAVEWATCH III version 1.15 for a global domain. NOAA/NWS/NCEP/OMB Technical Note 213, 33 pp.
- WAMDI group, 1988. The WAM model—a third generation ocean wave prediction model. *J. Phys. Oceanogr.*, 1775–1810.
- Weller, R.A., Price, J.F., 1988. Langmuir circulation within the oceanic mixed layer. *Deep-Sea Res.* 35, 711–747.
- Welsh, D.J.S., Bedford, K.W., Wang, R., Sadayappan, P., 2000. A parallel-processing coupled wave/current/sediment transport model. Technical Report ERDC MSRC/PET TR/00-20, US Army Engineer Research and Development Center, Vicksburg, MS.
- Whitham, G.B., 1965. A general approach to linear and non-linear dispersive waves using a Lagrangian. *J. Fluid Mech.* 22, 273–283.
- Wu, J., 1982. Wind-stress coefficients over sea surface from breeze to hurricane. *J. Geophys. Res.* 87, 9704–9706.
- Xie, L., Wu, K., Pietrafesa, L., Zhang, C., 2001. A numerical study of wave–current interaction through surface and bottom stresses: wind-driven circulation in the South Atlantic Bight under uniform winds. *J. Geophys. Res.* 106 (C8), 16841–16855.
- Xie, L., Pietrafesa, L.J., Wu, K., 2003. A numerical study of wave–current interaction through surface and bottom stresses: coastal ocean response to Hurricane Fran of 1996. *J. Geophys. Res.* 108 (C2), 3049, doi: [10.1029/2001JC001078](https://doi.org/10.1029/2001JC001078).
- Yanagi, T., Takahashima, S., 1993. Seasonal variation of circulations in the East China Sea and the Yellow Sea. *J. Oceanogr.* 49, 503–520.
- Zhang, M.Y., Li, Y.S., 1996. The synchronous coupling of a third-generation wave model and a two-dimensional storm surge model. *Ocean Eng.* 6, 533–543.
- Zhang, M.Y., Li, Y.S., 1997. The dynamic coupling of a 3rd-generation wave model and a 3d hydrodynamic model through boundary-layers. *Cont. Shelf Res.* 17, 1141–1170.